

Learning functional groups in complex microbiomes

Matthew S. Schmitt^{1,2*}, Kiseok K. Lee^{3,4,5*}, Freddy Bunbury^{3,4,5}, Joseph A. Landsittel⁶, Vincenzo Vitelli^{1,2,5,7,8**}, Seppe Kuehn^{3,4,5,8**}

¹James Franck Institute, University of Chicago, Chicago, Illinois 60637, U.S.A.

²Department of Physics, University of Chicago, Chicago, IL 60637, U.S.A.

³Department of Ecology and Evolution, University of Chicago, Chicago, IL 60636, U.S.A.

⁴Center for the Physics of Evolving Systems, University of Chicago, Chicago, IL 60636, U.S.A.

⁵Center for Living Systems, University of Chicago, Chicago, IL 60636, U.S.A.

⁶Department of Engineering Sciences and Applied Mathematics, Northwestern University, Evanston, IL, U.S.A

⁷Leinweber Institute for Theoretical Physics, University of Chicago, Chicago, IL 60637, U.S.A.

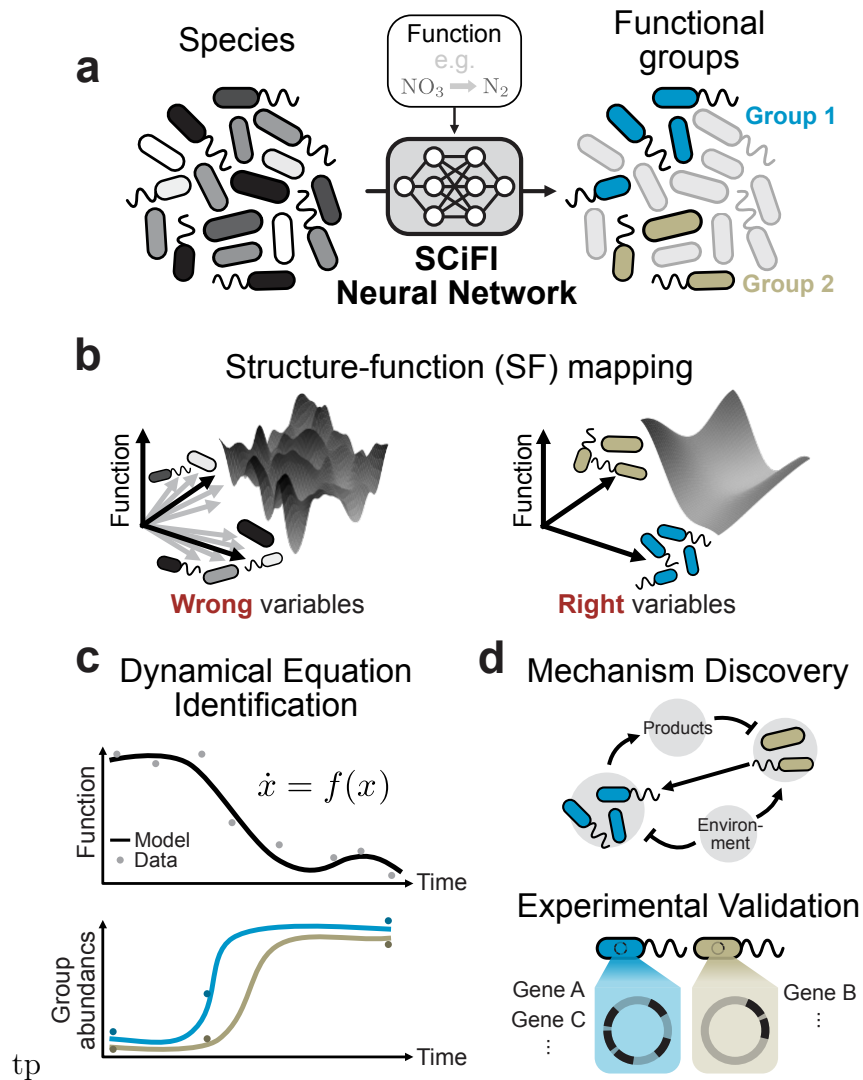
⁸National Institute for Theory and Mathematics in Biology, Northwestern University and University of Chicago, Chicago, IL, U.S.A.

* These authors contributed equally

** Correspondence: vitelli@uchicago.edu, seppe.kuehn@gmail.com

1 ABSTRACT

2 From soil to the gut, communities composed of thousands of microbes perform functions such as
3 carbon sequestration and immune system regulation. Here, we introduce a data-driven approach
4 that explains how community function can be traced to just a few groups of microbes or genes. In
5 gut communities, our neural-network based clustering algorithm correctly recovers known functional
6 groups. In the ocean metagenome, it distills ~ 500 gene modules down to three sparse groups
7 highlighting survival strategies at different depths. In soils, it distills ~ 4400 bacterial species into two
8 groups that enter a mathematical model of nitrate metabolism. By combining interpretable ML with
9 strain isolation and sequencing experiments, we connect the metabolic specialization of each group
10 to community-wide responses to perturbations. This integrated approach yields simple structure-
11 function maps of microbiomes, allowing the discovery of molecular mechanisms underlying human
12 and environmental health. More broadly, we illustrate how to do function-informed dimensionality
13 reduction in biology.



Graphical Abstract: An integrated ML and experimental pipeline to discover functional groups and their dynamics in complex microbiomes and beyond. (a) First, our Soft Clustering Function Informed (SCiFI) algorithm identifies functional groups directly from species abundances data using neural networks. Crucially, the learned functional groups are informed by a chosen community function. (b) Descriptions of the system in terms of the original high-dimensional abundances of individual species are prohibitively complex (left). By contrast, a description in terms of the few functional groups identified by SCiFI leads to a simple structure-function map (right). (c) Next, the identified groups can be directly input as variables into predictive mathematical models for the dynamics of the community. (d) The last step of our pipeline relies on the identified groups comprising only a small number of species. This sparsity enables targeted experiments that interrogate isolated species (e.g. with whole-genome sequencing or phenotyping) shedding light on the mechanistic underpinnings of the structure-function map with potential applications beyond microbiomes, from gene expression to neuronal activity.

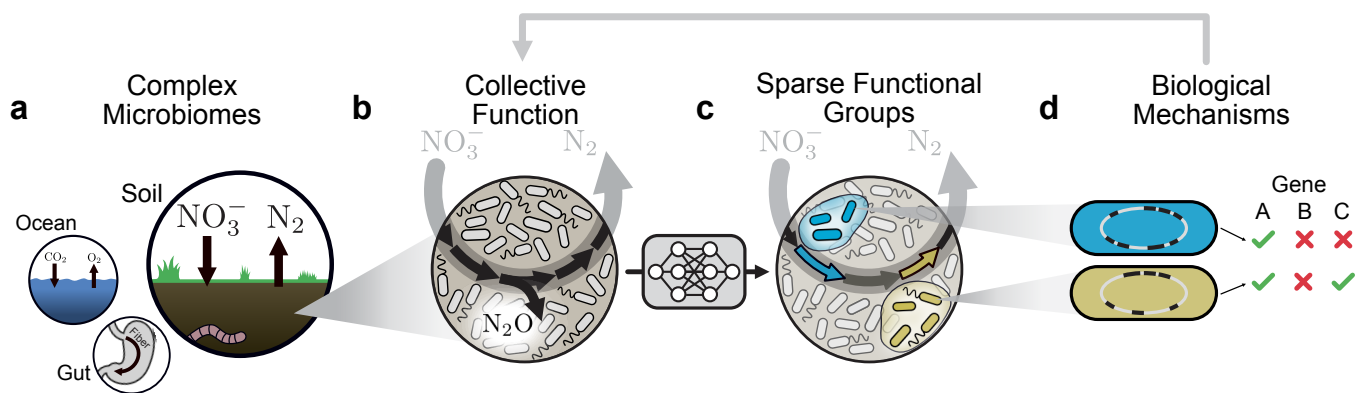


Figure 1: Data-driven discovery of functional groups and their dynamics (a) Microbial communities perform crucial environmental functions from the soil to the ocean to the gut. (b) In soils, microbes collectively reduce nitrate to dinitrogen gas in a process called denitrification. This process is composed of several discrete steps (black arrows), one of which produces the potent greenhouse gas nitrous oxide. (c) Our machine learning method, SCiFI, automatically finds the functional groups of bacteria (blue, green) that contribute to community function. These groups correspond to distinct metabolic functions (arrows). (d) By sequencing the genomes of group members, we can disentangle the biological mechanisms leading to collective function.

14 INTRODUCTION

15 Bacteria account for $\sim 10\%$ of all biomass on earth [1]. Collectively, they perform important
 16 metabolic functions such as transferring gigatons of carbon [2–4] and nitrogen [5] between the
 17 soil and the atmosphere every year, clearing pollutants from wastewater [6], and protecting against
 18 pathogen colonization [7]. These functions arise from the concerted metabolic activity of structured
 19 communities consisting of hundreds or thousands of individual species. This complexity makes the
 20 corresponding structure-function mapping difficult to decipher.

21 However, the biochemistry of metabolism suggests that the composition of a bacterial community
 22 and its relationship to function can be described in terms of just a few functional groups that perform
 23 distinct roles [8–15]. How can we distill these groups automatically from data and mechanistically
 24 relate them to community function?

25 As an example, consider the microbiome function triggered when you put fertilizer in damp
 26 soil (Fig. 1a). The metabolic process of denitrification, responsible for significant greenhouse gas
 27 emissions, rapidly ensues [16, 17]. The greenhouse gas nitrous oxide (N_2O) is emitted by the
 28 collective action of functional groups, each specialized in specific steps of the metabolic cascade,
 29 e.g. conversion of NO_3^- (fertilizer) to N_2O or of N_2O to N_2 (Fig. 1b) [18]. Identifying functional
 30 groups, and their role in the community, has traditionally required extensive experimental studies
 31 of isolates and their interactions [19, 20].

32 Here, we introduce a machine-learning algorithm called SCiFI that discovers functional groups
 33 from data, yielding interpretable structure-function maps for complex microbiomes (Fig. 1c). A
 34 key finding is that each functional group contains only a few relevant members. By experimentally
 35 targeting this subset of bacterial species we can rapidly evaluate the biological mechanisms defining
 36 each group’s role in community function (Fig. 1d). In soil, this integrated machine-learning and
 37 experimental approach reveals how the members of two genetically distinct groups collectively
 38 determine denitrification dynamics across varying environments.

39 RESULTS

40 A machine learning approach to function-informed clustering: the SCiFI algorithm

41 Our goal is to distill a small number of functional groups from abundance measurements of thou-
42 sands of microbial species in a way that is informed by community function. The task of aggregating
43 species into groups is an instantiation of a more general one called dimensionality reduction: obtain-
44 ing a low-dimensional representation of a complex system that retains its salient features. Unlike
45 physical systems that are often representable by a single set of collective variables governing their
46 behavior (e.g. P , V , T for a gas), biological systems do not typically possess a unique decomposition
47 into collective variables. In proteins, for instance, the groups of residues governing thermal stability
48 are distinct from those governing catalytic activity [21] while in cells, the genes that control dif-
49 ferentiation into fibroblasts are not those controlling differentiation into neurons [22]. Similarly, in
50 microbiomes the groups relevant for denitrification [19] differ from those relevant for methanogenesis
51 [23]. Nevertheless, with few exceptions [24, 25], dimensionality reduction in microbiomes is typically
52 attempted without explicitly linking groups and function [26–28]. Species are first clustered into
53 groups via statistical or genomic methods, and only later the resulting groups are correlated with
54 function [29–31].

55 Here, we introduce a machine learning algorithm that simultaneously identifies groups and as-
56 sociates them with collective function. Our soft clustering function-informed (SCiFI) algorithm
57 exploits a Gumbel softmax trick that turns cluster identity (typically a categorical variable) into
58 a continuous (i.e., soft) variable (Methods). This continuous representation, beyond enabling the
59 model to express uncertainty, is fully differentiable. Hence, optimization can be performed with
60 gradient descent which allows information to flow, via gradients, from function to clustering. This
61 crucial feature is what allows SCiFI to find groups that are informative of specific functional pro-
62 cesses.

63 Figure 2a describes SCiFI in a nutshell, emphasizing how it simultaneously yields the group
64 identification (left) and the structure-function map (right). The input is community structure,
65 represented as a species abundance vector (gray). The output is a prediction of function (blue),
66 which may be a vector (e.g. a time series of metabolite concentration) or a scalar (e.g. the concen-
67 tration at a single time point). To go from input to output, we first group species by multiplying
68 the abundance vector with an interpretable clustering matrix: each row of this matrix encodes
69 by construction the group assignment for one species (Methods). This aggregation of species by
70 summation assumes that members within a group are indistinguishable. In systems with a large
71 number of species many are irrelevant for function prediction. In such cases, we encourage SCiFI
72 to find sparse groups, i.e. comprising only a few species, with an optional gating step achieved via
73 regularization and presented in details in Methods. The resulting group abundances are in turn
74 fed to a neural network (green) that maps them to function. The neural network enables SCiFI to
75 accommodate nonlinear structure-function maps which, as we show below, occur in real systems.
76 SCiFI updates both the clustering matrix and the neural network parameters (blue arrows) to mini-
77 mize the deviation between predicted and true function. Simultaneous updating is the architectural
78 feature that ensures feedback between clustering and structure-function mapping during training.
79 This is how SCiFI’s groups become function informed.

80 We benchmark SCiFI using a simulated dataset (Methods) where function is generated from a
81 small number of groups through a nonlinear structure-function map (Fig. 2b). Nonlinearity is a
82 typical feature of the experimental microbiome datasets we analyze below. For benchmarking we
83 consider other models that can be used to find functional groups. Each of these models lack one
84 or both of the SCiFI’s defining features, namely its nonlinearity and function-informed clustering

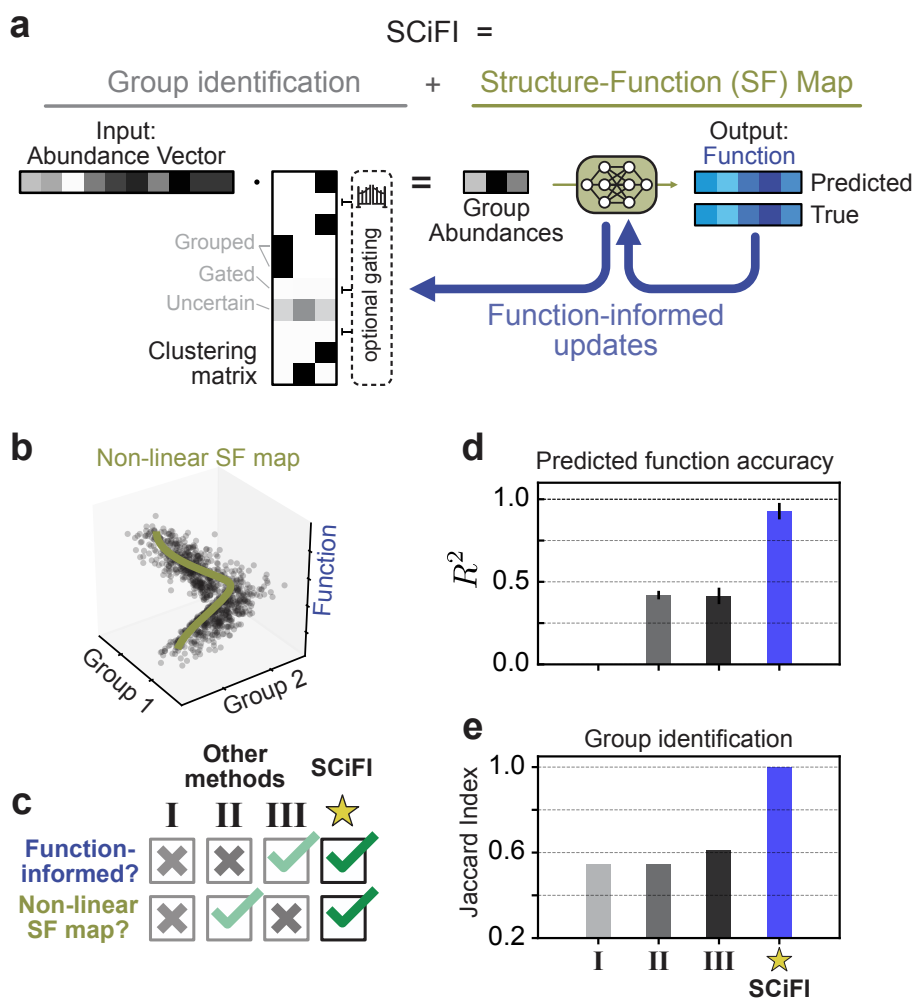


Figure 2: SCiFI: a neural network-based method to identify functional groups (a) Our pipeline consists of two steps: first, species abundances are aggregated via matrix multiplication with a grouping matrix; second, group abundances are used to predict the target function using a neural network. An optional gating term allows entire rows of the grouping matrix to be set to zero (Methods). During training, the grouping matrix is learned simultaneously with the neural network using gradients from the loss function. (b) A simple model of nonlinear data, in which the function depends on the inputs only through grouped abundances (Methods). (c) We compare our method to three alternative models which lack SCiFI’s ability to capture a non-linear function map, find function-informed clusters, or both. Each method is described in the main text. (d) R^2 of function predictions on a held-out subset of the data for each method. (e) Group recovery for each method as measured by Jaccard Index (Methods).

85 (Fig. 2c). Model I learns a grouping independent of function by first clustering with a co-occurrence
86 network and then predicting the function from group abundances with linear regression [29]. Model
87 II performs the same first abundance-based clustering step, but uses a neural network to learn
88 the mapping between group abundances and function. Finally, Model III, introduced in Ref. [25],
89 learns a function-informed clustering with a Monte Carlo approach combined with a linear structure-
90 function mapping.

91 SCiFI accurately predicts function (Fig. 2d) and recovers functional groups as measured by the
92 Jaccard score (Fig. 2e and SI Figs. S3, S4), which computes the ratio of correct group classification
93 to the total group size. Benchmarking reveals that these models generally fail to recover the correct
94 groups and predict function (Fig. 2d-e). Models I and II fail because they first misidentify groups,
95 which then inhibits function prediction. In Model III the situation is reversed: its inability to
96 predict nonlinear function leads it to incorrectly identify groups (SI Fig. S5).

97 **SCiFI algorithm correctly identifies functional groups for *in vitro* gut microbiomes**

98 We validate SCiFI’s performance on synthetic gut microbiome experiments from Ref. [32], which
99 form communities consisting of combinations of 30 gut bacteria. This dataset consists of hundreds
100 of paired measurements of strain abundances and fermentation products relevant for gut health
101 including butyrate and succinate.

102 We first aim to identify functional groups relevant for butyrate production. The correct number
103 of groups is *a priori* unknown. To find it, we train multiple networks over a range of possible group
104 numbers N_{groups} and see when the error in butyrate prediction stops decreasing (Fig. 3a). Because
105 the number of species is small, we do not require SCiFI’s optional gating step. We find that four
106 functional groups are necessary to accurately predict butyrate production of the whole community.
107 The groups we learn are robust (SI Figs. S6, S7) and interpretable in terms of the phenotypes de-
108 scribed in Ref. [32] (Fig. 3b and SI Fig. S8). The first group contains a single member, *Anaerostipes*
109 *caccae* (AC) a butyrate producer which can switch between low butyrate (sugar-utilizing butyrate
110 production) and high butyrate (lactate-utilizing butyrate production) producing states depending
111 on environmental pH [32]. This explains the second group of so-called “pH buffers”, which are species
112 that are highly correlated with pH that modulate butyrate production by impacting AC’s mode of
113 production (SI Fig. S9a). The third group contains the rest of the direct butyrate producers, while
114 the final group contains the remaining species which are not important for butyrate production.
115 These groups, which were independently experimentally confirmed in Ref. [32] show that SCiFI
116 correctly learns functional groups in the microbiome.

117 Knowledge of these four coarse-grained groups suffices to accurately predict butyrate concentra-
118 tion (Fig. 3c). This is possible only because SCiFI can learn non-linear structure-function relation-
119 ships. If the non-linearity is removed and we instead use linear regression to predict butyrate from
120 the (learned) group abundances, the model suffers a significant decrease in accuracy (Fig. 3d and
121 SI Fig. S10).

122 Repeating our analysis using succinate concentration instead of butyrate results in a completely
123 different group structure (Fig. 3e-f). SCiFI correctly ignores the dominant species (measured by
124 average abundance) AC, and instead isolates strains from the *Bacteroidetes* phylum. In contrast
125 to the butyrate case, the loss continues to see modest decreases as we increase the number of
126 groups beyond the initial plateau (at $N_{\text{cluster}} = 2$) which correspond to subsequent subdivisions of
127 *Bacteroidetes*.

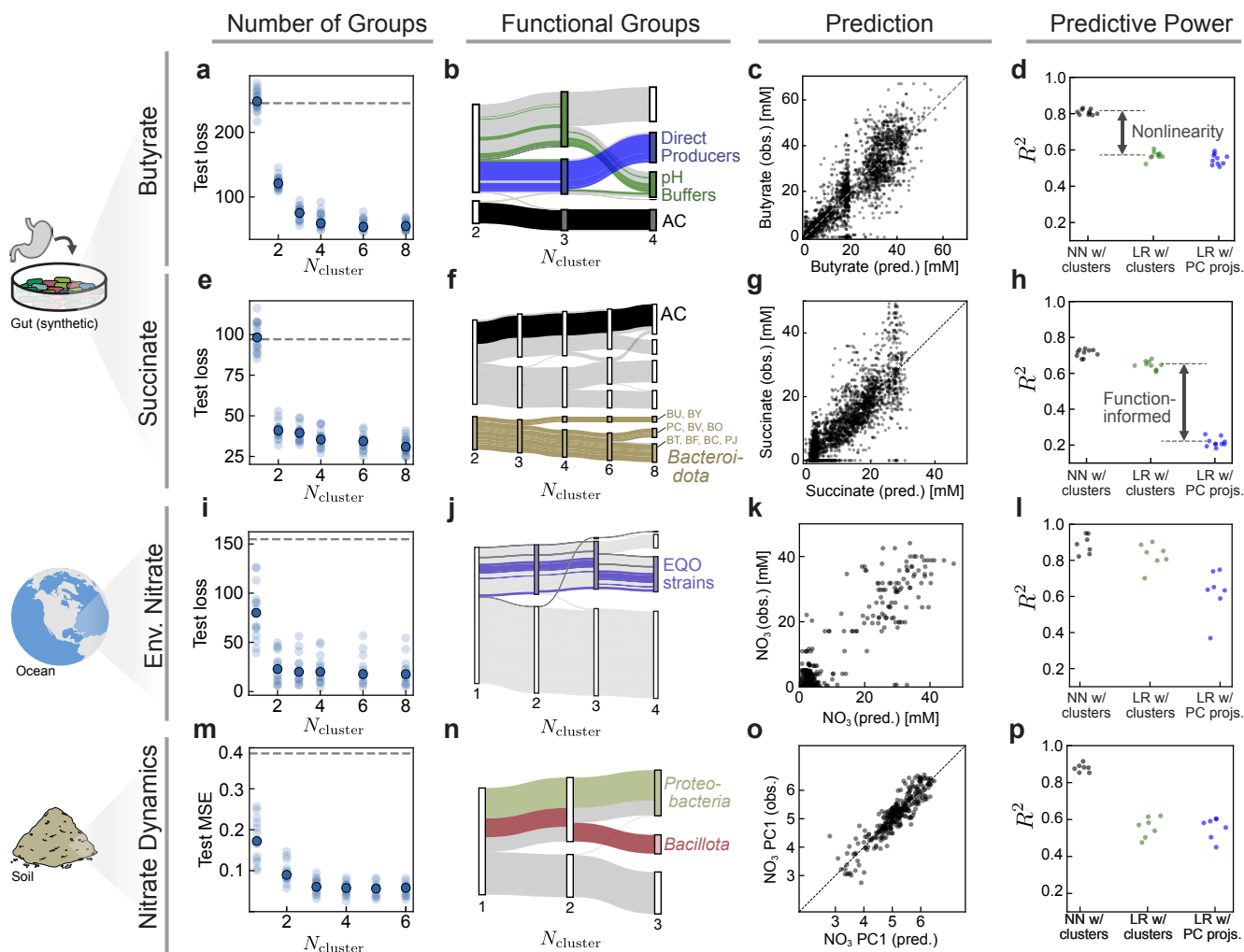


Figure 3: SCiFI correctly learns functional groups in the gut, soil, and ocean microbiome

(a) We train our model to predict butyrate production based on the abundances of 30 bacterial strains in synthetic gut communities (data from Ref. [32]). Test loss (mean squared error) of predicted butyrate concentrations is shown for varying numbers of functional groups N_{cluster} . Each faint dot is one model trained with one particular test/train split of the data. The solid dot shows the median across the entire ensemble of models ($N = 12$ test/train splits total). Dashed gray line shows the variance of butyrate as a reference. (b) Flow chart showing how group structure changes with varying N_{cluster} . Thickness of each bar corresponds to the average abundance of that species across the dataset. Several individual species are highlighted; for interpretation see the main text. (c) SCiFI predictions (with $N_{\text{cluster}} = 4$) versus observed butyrate concentrations in each sample. (d) Comparison of test-set R^2 values for three models: the neural network which uses the identified cluster abundances as inputs; a linear regression which uses the cluster abundances as inputs; and a linear regression which uses the projection onto the first 4 principal components as inputs. Each point is a model trained and evaluated using a different test-train split of the data (Methods). All models use a 4-dimensional input (that is, either $N_{\text{clusters}} = 4$ or $N_{\text{PCs}} = 4$). (e-h) Same plots as in the top row, using succinate as the target function. The models in (g) and (h) use $N_{\text{clusters}} = 2$. (i-l) Results for genus abundances in marine communities. Target function is a scalar measurement of environmental nitrate concentration. The models in (k) and (l) use $N_{\text{clusters}} = 2$. (m-p) Results for phylum abundances in soil communities. Target function is a time-series of nitrate concentrations. The models in (o) and (p) use $N_{\text{clusters}} = 3$. All of these models in this figure are trained without the optional gating step described in Figure 2a. For each dataset, a comparison to several other methods may be found in SI Fig. S10.

128 How can we understand how the learned groups contribute to community function? To move
129 forward we use the learned groups as the starting point for a genomic analysis. Namely, we use
130 sequenced genomes of group members to search for key enzymes that produce succinate using the
131 Biocyc database [33]. This reveals that all nine strains assigned to the putative succinate-producing
132 group (brown in Fig. 3f) have at least one copy of the fumarate reductase gene. By contrast, all
133 other strains lack fumarate reductase except for the two species EL and FP, which have low average
134 abundance (SI Fig. S9b).

135 In contrast to the butyrate case, the relationship between the functional groups and succinate
136 prediction is simple: a linear model predicts succinate from the group abundances nearly as well
137 as the neural network (Fig. 3g; green in Fig. 3h). However, this is only true when the clustering is
138 function-informed. If we instead project the abundance data onto its principal components (blue)
139 as opposed to our function-informed clustering matrix, a linear model is incapable of predicting
140 succinate concentration. This indicates that the dominant variance in abundances does not re-
141 flect changes in succinate concentration and highlights the importance of identifying clusters in a
142 function-informed manner.

143 In summary, because it is function-informed, SCiFI can identify multiple different groupings
144 from the same set of abundance data. Further, the groups that we learn have clearly interpretable
145 biological roles, and in the case of succinate they also possess a distinct genetic signature.

146 **SCiFI finds functional groups in natural ocean and soil microbiomes.**

147 In contrast to the synthetic communities above, in natural ocean and soil samples the experimen-
148 talist has little to no control over the composition of the community. Our method identifies relevant
149 functional groups even in these settings.

150 First, we aim to find functional groups in the ocean microbiome using the Tara Oceans dataset
151 [34, 35]. In this data we lack access to the functional outputs of the community: we cannot
152 measure how much nitrate is being dynamically consumed, only the steady state concentration. We
153 nevertheless treat the environmental variables as a proxy for functional measurements, and train our
154 networks to predict sample nitrate concentrations. Two groups suffice to accurately predict nitrate,
155 and we find that the structure-function map is well-approximated by a linear model (Fig. 3i-l and
156 SI Fig. S10). Because we lack a ground truth in this case, we confirm that our learned functional
157 groups contain all strains identified by an alternative method (Ensemble Quotient Optimization;
158 EQO) introduced in Ref. [24]. Like EQO, SCiFI produces a group consisting of “complementary”
159 (anti-correlated) species, but in contrast to EQO it does so without having this feature built in the
160 objective function (SI Fig. S8).

161 Finally, we consider soil microcosm experiments from Ref. [36] which measure nitrate reduction
162 dynamics together with the end-point phyla abundances under a range of pH perturbations. In
163 contrast to the previous examples, function is a vector representing the concentration of nitrate over
164 time. Our method indicates that three functional groups, which in particular isolate Proteobacteria
165 and Bacillota, are necessary to predict nitrate dynamics (Fig. 3m-p). This is consistent with previous
166 work showing the key role of members of these phyla in governing denitrification in soils subjected
167 to basic perturbations [36]. These groups are sufficient to predict nitrate consumption only if the
168 structure-function map is nonlinear (Fig. 3o-p and SI Fig. S10).

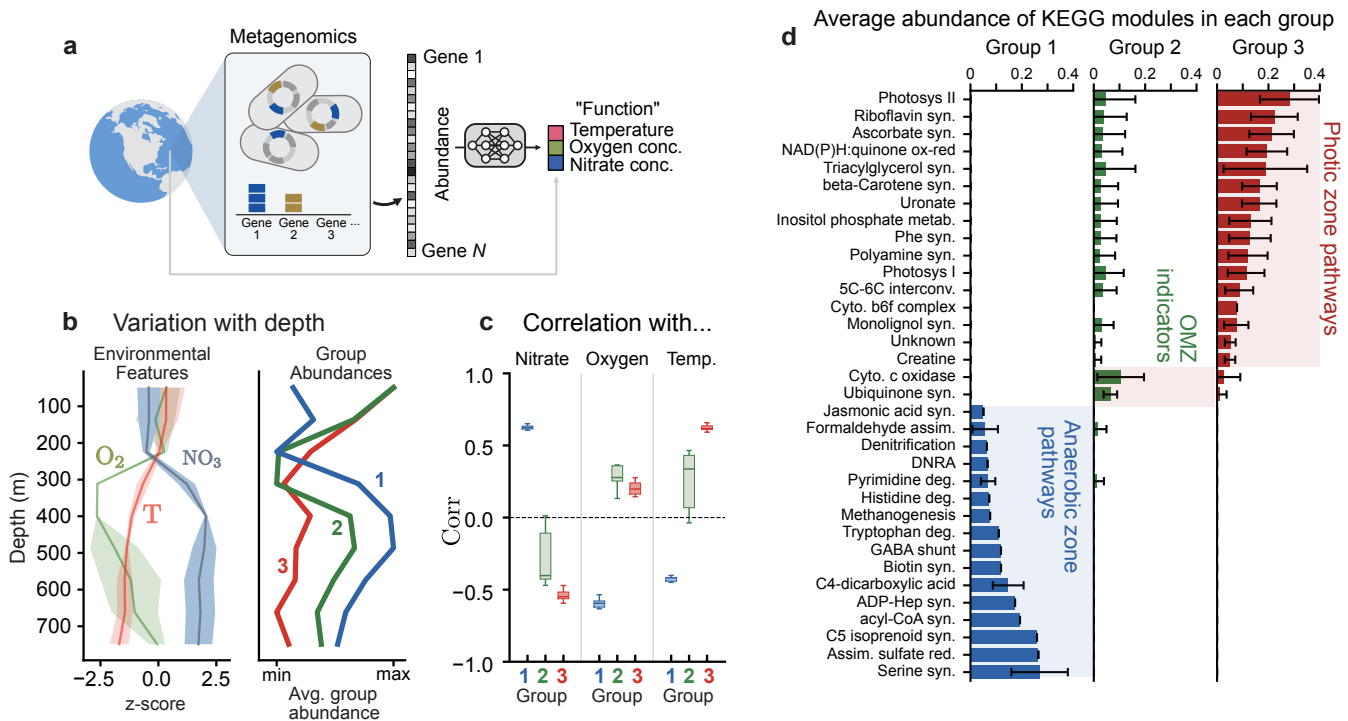


Figure 4: Sparse functional gene groups reveal survival strategies in the ocean microbiome

(a) We use SCiFI to cluster gene modules using environmental parameters as a proxy for function. Structure in this dataset is quantified via shotgun metagenomics which quantifies the abundances of different genes across all genomes in the sample. Environmental variables include both those related to community function (e.g. oxygen, nitrate concentrations) and to abiotic forcing (e.g. temperature). (b, left) Average nitrate concentration, oxygen concentration, and temperature as a function of depth. Quantities are normalized to have mean zero and standard deviation of one. (b, right) Average group abundance for the three groups identified with our algorithm, normalized by max/min. (c) Correlation of group abundances with each of the three environmental parameters used as target function during training: nitrate, oxygen, and temperature. (d) Allocation of several selected KO pathways to our learned groups. Bar heights denote the average abundance of each module assigned to each group. Average is taken across samples and across 12 test-train splits of the dataset; error bars show one standard deviation across test-train splits.

169 SCiFI distills groups of genes in the ocean metagenome

170 Nothing about SCiFI limits its applicability to clustering species – it just as readily clusters genes.
 171 We now demonstrate this capability by finding relevant groups of genes present in microbial com-
 172 munities in the world’s oceans. The Tara Oceans dataset [34] provides measurements of gene
 173 abundances, which we consider aggregated at the level of KEGG modules [37, 38], and environmen-
 174 tal conditions at ~ 100 sites across the global ocean (Fig. 4a). The large number of gene modules
 175 (~500) poses a challenge to interpreting the resulting groups because even if there are a small num-
 176 ber of groups, they will be composed of a large number of genes. Here, we employ SCiFI’s optional
 177 gating procedure to achieve an approximate twenty-fold reduction in the number of relevant genes,
 178 which facilitates interpretation of their individual roles.

179 Similarly, nothing about SCiFI limits its applicability to clustering based on function alone –
 180 it can also incorporate the role of abiotic forces. The Tara data includes abiotic factors known to
 181 structure marine microbiomes, such as temperature [35]. To account for the impact of this key
 182 abiotic factor in metabolic function, we ask SCiFI to predict temperature along with oxygen and

183 nitrate concentrations. Three groups suffice to make accurate predictions (Fig. 4b; SI Fig. S11).
184 Two groups are strongly correlated to nitrate concentration (blue; group 1) and temperature (red;
185 group 3) (Fig. 4c), while the third (green; group 2) shows clear depletion at the transition to the
186 oxygen minimum zone.

187 After the sparsity promoting (gating) step, each group consists of only a small number of gene
188 modules Fig. 4d (also SI Figs. S12, S13). This allows us to interpret how the enrichment of groups
189 at certain depths (Fig. 4b) corresponds to different survival strategies. For example, group 1, which
190 is abundant in deep waters, contains modules for respiration with alternative electron acceptors
191 (nitrogen, sulfur). More interestingly, it also contains modules related to degradation of pyrimidine,
192 histidine, and tryptophan. This suggests that the bacteria residing in the nutrient poor conditions
193 of the deep ocean survive by scavenging nucleotides and amino acids for energy and growth. Group
194 3, in contrast, contains several gene modules related to protective compounds such as pigments
195 (beta-Carotene), protective vitamins (ascorbate) and exopolysaccharide (uronate pathway), a key
196 component of biofilms [39, 40]. These compounds might reflect adaptations to the high stress that
197 surface bacteria experience at the surface due to UV radiation [41] or phage predation [42].

198 **SCiFI learns functional groups that are dynamical variables of mathematical models**

199 Up to now, we have interpreted the functional groups learned by SCiFI by looking at the phenotypes
200 of group members, their phylogeny, or in the case of clustering metagenomes, the function of proteins
201 those genes encode. However, this analysis does not reveal how the groups work together to drive
202 community function since the structure-function map is encoded by a neural network that is not
203 readily interpretable. We now show that the functional groups learned by SCiFI can be directly
204 used as variables in a fully interpretable mathematical model that relates groups to community
205 function.

206 As an example, we consider how nitrate utilization in soil microbiomes is impacted by short
207 and long-term changes in soil pH, a key environmental variable [36, 43]. Previous work has shown
208 that a consumer-resource model predicts the dynamics of nitrate utilization (the resource) from
209 a single effective biomass (the consumer) [36]. The model parameters, including the size of the
210 effective biomass, were inferred from the nitrate measurements alone. The approach revealed broad
211 mechanisms of pH induced changes in function, but did not provide a principled way to identify the
212 relevant bacteria from sequencing measurements. Here we show that SCiFI solves this problem.

213 We train SCiFI to predict trajectories of nitrate concentration using a vector of 4395 amplicon
214 sequence variant (ASV) abundances as input. This data comes from experiments which measure
215 the consumption of amended nitrate over time in soil samples collected across a natural pH gra-
216 dient (Methods). ASV abundances are measured at the initial and final time points. Samples are
217 subjected to a range of pH perturbations and incubated with and without a growth inhibiting drug
218 (chloramphenicol), yielding a total of ~ 750 microcosms (Methods).

219 We find that, with gating, two groups suffice to predict nitrate dynamics across the entire dataset
220 (SI Fig. S14, S15). To capture how the groups learned by SCiFI collectively consume nitrate, we
221 augment the consumer-resource model proposed in Ref. [36]:

$$\dot{x}_i = \gamma_i r_i x_i \frac{A}{A + K_A} \frac{C}{C + K_C}, \quad i = 1, 2 \quad (1)$$

$$\dot{A} = -(r_1 x_1 + r_2 x_2) \frac{A}{A + K_A}. \quad (2)$$

222 The two biomasses x_1 and x_2 are readily identified as the learned functional groups which consume
223 nitrate A with yields γ_i (1/mM) and at rates r_i (mM/day) which vary with pH. Biomass growth

233 SCiFI guides targeted experiments that reveal biological mechanisms

234 The two functional groups we find exhibit distinct dynamical behaviors (Fig. 5b). What is the
235 biological explanation for this difference? SCiFI by itself does not answer this question. However,
236 it does perform the first step of an integrated pipeline that combines machine learning with exper-
237 iments to reveal underlying biological mechanisms. Concretely, our approach exploits the sparse
238 groups learned by SCiFI to guide targeted experiments on representative species.

239 For nitrate reduction in soil, we seek a genetic explanation. This choice is motivated by the
240 fact that genes encode nitrate utilization traits of individual species [45]. We isolated a dominant
241 strain from each group (*Neobacillus fumarioli* from Group 1; *Peribacillus simplex* from Group 2)
242 and sequenced their genomes (Methods). These strains were selected because they were among the
243 most abundant in their respective groups. Because these strains differ only at the genus level, the
244 distinction between them would not have been discovered without function-informed clustering.

245 Whole genome sequencing of these isolates revealed that, despite their taxonomic proximity,
246 these strains differ in the denitrification enzymes they harbor (Fig. 6a). While the *Neobacillus*
247 strain (blue) possesses a complete set of genes to reduce nitrate to dinitrogen, the *Peribacillus* strain
248 (red) can only perform the intermediate step of reducing nitrite to nitric oxide. In Figure 6b we
249 show the inferred genomes of all group members (PiCRUSt2, [44]) sorted by their average absolute
250 abundance (right). We observe the same pattern: the most abundant Group 1 strains (blue) often
251 have a full set of genes required to convert nitrate to dinitrogen, while Group 2 strains perform only
252 partial steps in the pathway (Fig. 6b).

253 This finding allows us to explain how the nitrate reduction capacity of a community changes in
254 response to pH perturbations. In growth-inhibited conditions we observe that acidic soils ($\text{pH} \lesssim 6$;
255 gray in Fig. 6c) show robust nitrate reduction which is constant over a range of pH perturbations,
256 while neutral soils ($\text{pH} \gtrsim 6.5$; green in Fig. 6c) are more pH-sensitive. These two soil types differ
257 also in their composition: Group 1 dominates acidic soils, while Group 2 dominates neutral soils
258 (Fig. 6d).

259 Taken together, these observations suggest the following mechanism to explain community sen-
260 sitivity to pH perturbations. Neutral soils are characterized by a large population of Group 2,
261 which reduces nitrate by splitting the pathway among several different constituent strains. Such
262 cross-feeding communities are susceptible to nitrite toxicity at low pH [46], which slows the overall
263 utilization of nitrate (Fig 6e, left). Acidic soils, by contrast, are dominated by Group 1 which is
264 expected to fully reduce nitrate to dinitrogen and relieve nitrite toxicity, resulting in robustness to
265 pH perturbations (Fig. 6e, right). Both behaviors persist in growth conditions (SI Fig. S17). Our
266 integrated pipeline reveals how collective function depends on the differential response of individual
267 groups to perturbations.

268 DISCUSSION

269 It has been known since the Babylonians first made sourdough that communities of bacteria perform
270 important macroscopic functions. Only in the last century was it discovered that these communities
271 are composed of groups, or guilds, of microbes with similar metabolic strategies. The challenge for
272 microbiologists ever since has been to identify these strategies and disentangle their contributions to
273 collective metabolism. A common approach to identify groups and their strategies uses enrichment
274 cultures. For example, incubating a soil community in nitrate-rich, anoxic conditions will enrich
275 microbes that perform nitrate reduction. Genomics provides an alternative route to identify groups
276 in natural settings based on the presence or absence of genes that encode for functionally-relevant
277 enzymes. Neither of these approaches, however, quantitatively identifies a microbe's contribution to

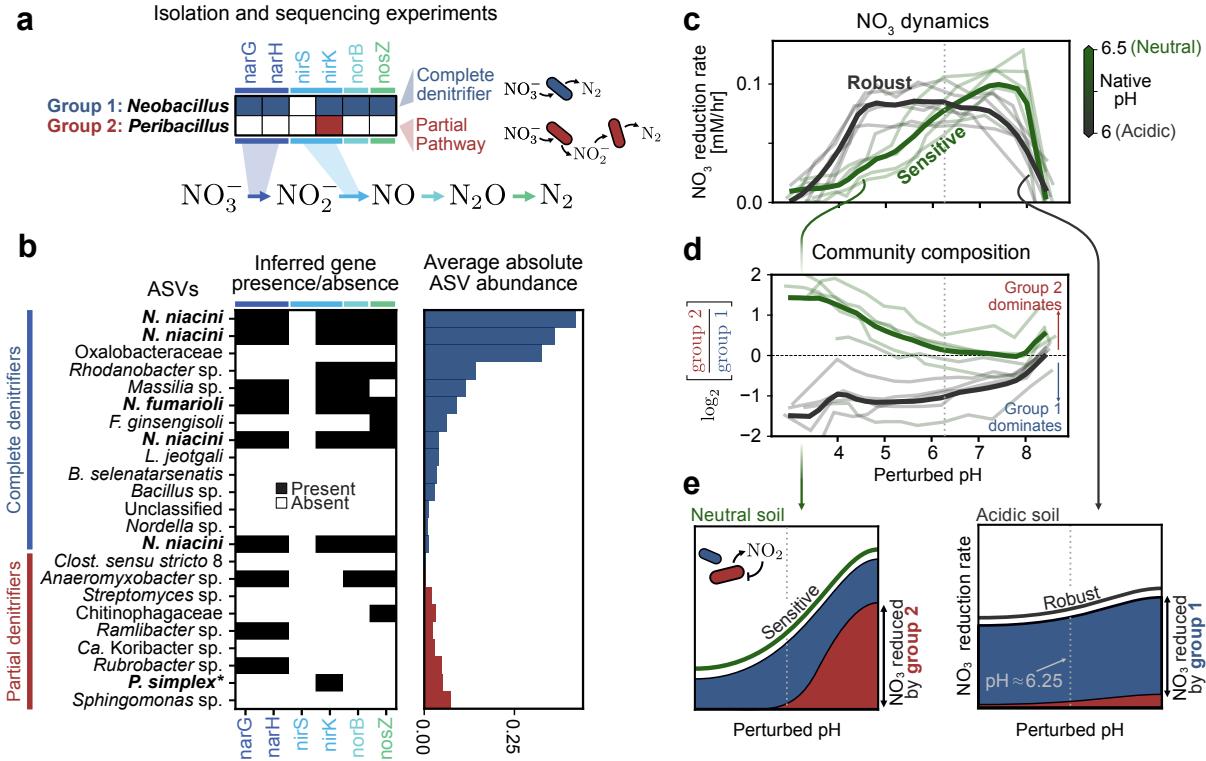


Figure 6: Functional groups reveal mechanistic underpinnings of pH sensitivity in soil communities (a) Whole genome sequencing of two isolates from the groups shown in (b) with the denitrification relevant enzymes they possess. *Neobacillus* has enzymes to perform all steps in the cascade (bottom), while *Peribacillus* can only perform the second step. (b, left) Denitrification gene presence (black) and absence (white) for individual ASVs in group 1 and group 2. Gene presence for strains in the genera isolated in (a) is inferred from sequencing data, for all other strains we use PICRUSt2 [44]. (right) Average end-point abundance of the selected ASVs, where average is taken across all samples not subjected to growth inhibition via chloramphenicol. (c) Nitrate reduction rate (y -axis) of soils varies depending on perturbed pH (x -axis). Each faint line corresponds to one soil sample treated with chloramphenicol (non-treated samples are shown in SI Fig. S17). Solid lines correspond to the average when grouped by pH; acidic (gray) soils are those with native pH below 6.25, neutral (green) soils are those with pH greater than 6.25. In all panels in (c-e), the gray dashed vertical line denotes a perturbed pH of 6.25. (d) Variance of the community composition, as measured by log ratio between group 1 and group 2, as a function of perturbed pH. A value greater than 0 indicates that group 2 dominates, and a value less than zero indicates group 1 dominates. As in (c), faint lines indicate individual soils and solid lines are the average across acidic (gray) and neutral (green) soils. (e) Simple picture showing how the observed dependence of nitrate reduction on pH arises due to our two groups. (left) Neutral soils have, at neutral pH, a large contribution to nitrate reduction from both group 1 (blue) and group 2 (red). As pH is decreased, the contribution due to group 2 disappears because of nitrite toxicity (inset). (right) In acidic soils, only group 1 is present. Because it is a complete denitrifier, it is not sensitive to the buildup of nitrite and hence robustly reduces nitrate across all pH levels.

278 community function. Enrichment cultures necessarily remove microbes from their natural context
279 and hence do not capture how a microbe behaves when embedded in a complex community, while
280 genomics does not consider metabolite fluxes explicitly.

281 Our approach is not subject to these shortcomings because it learns functional groups directly
282 from data of natural communities. This success hinges on the fact that SCiFI is function-informed
283 and nonlinear. Because it is function-informed, we do not need experiments to be fine-tuned to
284 elicit the growth of one particular functional group. Instead, groups can be identified *post hoc* from
285 any experiment that generates correlations between abundances and function. Nonlinearity allows
286 SCiFI to capture interactions between groups, such as those between *A. caccae* and pH buffering
287 strains that modulate modes of butyrate production (Fig. 3a-d).

288 SCiFI can dramatically simplify the process of characterizing the structure of the community and
289 its relationship to function. Because it is function-informed, SCiFI can leverage a single experiment
290 that measures multiple functions to learn multiple groupings from the same abundance data. This
291 could dramatically reduce the number of experiments needed to characterize the structure of a
292 community.

293 Equation learning pipelines that build on SCiFI can explain the relationship between structure
294 and function. Here, we used SCiFI to extract the relevant variables for a consumer resource model
295 whose mathematical form was chosen based on intuition grounded in previous work [36]. However,
296 if we replace the neural network structure-function map with a sparse-regression model [47] or a
297 NeuralODE [48], the form of the mathematical model itself can be inferred directly from data with
298 little *a priori* knowledge.

299 Complex structure-function relationships are not unique to microbiomes. Our integrated pipeline
300 can find low-dimensional descriptions of structure in other contexts with no change to the core algo-
301 rithm. The underlying assumption behind SCiFI is that group members (of which bacterial species
302 are but an example) are indistinguishable and may meaningfully be aggregated by summation. Any
303 problem that has this feature may be tackled with our framework. We suggest two cases where this
304 assumption is likely to be fulfilled. First, SCiFI may be applied to neural firing rates to learn the
305 low-dimensional “neural manifold” underlying motor functions [49]. For example, a simple aggrega-
306 tion of (preprocessed) neural activity has been shown to predict the direction of rhesus monkey arm
307 movement from single-neuron data alone [50]. SCiFI could automate this aggregation procedure
308 and extend it to non-linear structure-function mapping. As a second example, SCiFI may be used
309 to understand the structure-function relationship between T-cell receptor sequence and immune
310 response. The immune response to a particular antigen is determined by the aggregated activity
311 of all T-cells which recognize it [51]. SCiFI could learn functional groups from experiments which
312 challenge a T-cell community with a complex pathogen (e.g. a whole virus) and measure their
313 collective response (e.g. total interferon γ production).

314 LIMITATIONS OF THE STUDY

315 SCiFI identifies groups based on a statistical relationship between abundances and function. How-
316 ever, it is not guaranteed that these groups are actually generators of function. This is a general
317 limitation of machine learning methods that can be ultimately traced to the fact that correlation
318 is not causation. While in every dataset we considered SCiFI learned biologically relevant groups,
319 this outcome ultimately needs to be independently checked either with mathematical modeling or
320 further experiments.

321 As a data-driven approach, SCiFI inevitably inherits the limitations of the dataset. Noise can
322 hinder SCiFI’s ability to find groups, especially groups that only weakly impact function. For

323 example, in a simulated linear degradation cascade where function is defined as the concentration
324 of the final product, groups that are far upstream are recovered imperfectly even though they are
325 biologically necessary (SI Fig. S4).

326 Finally, as described above, the grouping sought by SCiFI inherently assumes that species within
327 a group are indistinguishable. While this limits the class of problems to which it may be applied, it is
328 also crucial for the interpretability of our method. SCiFI may be adapted to allow for distinguishable
329 group members in a way analogous to how we introduced the gating to enforce sparsity. However,
330 this extension may come at the cost of reduced interpretability.

METHODS

Neural network details

Here we describe the architecture and training protocol of SCiFI in detail. Let us denote the abundance (row) vector for one sample by $x \in \mathbb{R}^n$ and the corresponding function (row) vector by $f \in \mathbb{R}^m$. To make a prediction of the function from the abundance data, SCiFI first computes group abundances $g \in \mathbb{R}^{N_{\text{clust}}}$ via the clustering matrix $C \in \{0, 1\}^{n \times N_{\text{clust}}}$, so that $g = xC$. (We discuss how the clustering matrix C is generated below.) From the group abundances, we predict the function with a neural network parameterized by parameters θ : $\hat{f} = \text{NN}_\theta(g)$. From this, we compute the mean squared error as our loss function

$$\mathcal{L}(C, \theta) = \frac{1}{B} \sum_{i=1}^B \|f_i - \hat{f}_i(x_i; C, \theta)\|^2 \quad (3)$$

where the sum is taken over samples in our batch B . In the case of minibatch gradient descent this is a random subset of the data, but due to the small number of samples in our datasets considered here we do not need to perform minibatching.

Gated SCiFI for sparse groups

The gating procedure described in the main text is easily incorporated as a step prior to the grouping. The gate is represented by a vector $\gamma \in (0, 1)^n$, and is applied to get the gated abundances $x^g = \gamma \odot x$, where \odot denotes element-wise multiplication. The gate is computed from a real-valued parameter $\ell_i \in \mathbb{R}$ via $\gamma_i = \text{sigmoid}(\ell_i)$ which allows us to learn it with standard gradient descent. From there, group abundances are computed as $g = x^g C$ and the following steps are unchanged. The loss function includes a term to enforce sparsity in the gate,

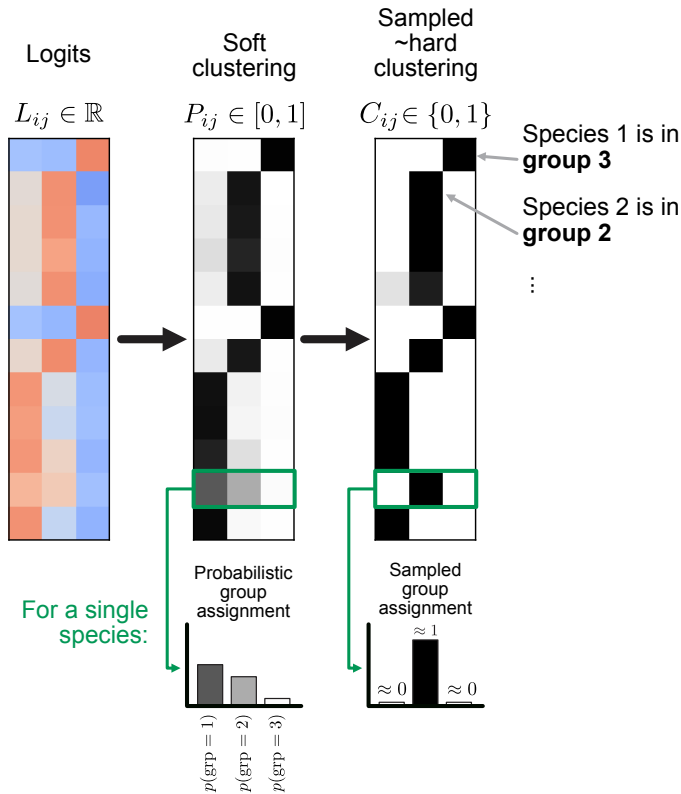
$$\mathcal{L}(C, \gamma, \theta) = \frac{1}{B} \sum_{i=1}^B \|f_i - \hat{f}_i(x_i; C, \gamma, \theta)\|_2^2 + \beta \|\gamma\|_1 \quad (4)$$

where here we distinguish between the 2-norm $\|\cdot\|_2$ and 1-norm $\|\cdot\|_1$. We introduce a new hyper-parameter β which controls how much we want to enforce sparsity; a large β leads to very sparse solutions, but typically there is a trade-off between sparsity and predictive accuracy.

Gumbel softmax for clustering

Here we explain how the Gumbel softmax trick may be used for clustering. The clustering problem is one of assigning a cluster index to every entry in our input vector. If $x \in \mathbb{R}^n$ is our vector of abundances, then the clustering is represented as a vector $\hat{c} \in \{1, \dots, N_{\text{clust}}\}^n$ where N_{clust} is the number of clusters, for example $\hat{c} = (1, 2, 1, 1, 3, 2)$ represents a clustering of 6 species into 3 clusters. Instead of representing the cluster identity as a (categorical) integer, we may equivalently represent it by a one-hot vector. The clustering is then given by a matrix $C \in \mathbb{R}^{n \times N_{\text{clust}}}$. The above example would be

$$C = \begin{pmatrix} 1 & 0 & 0 \\ 0 & 1 & 0 \\ 1 & 0 & 0 \\ 1 & 0 & 0 \\ 0 & 0 & 1 \\ 0 & 1 & 0 \end{pmatrix}.$$

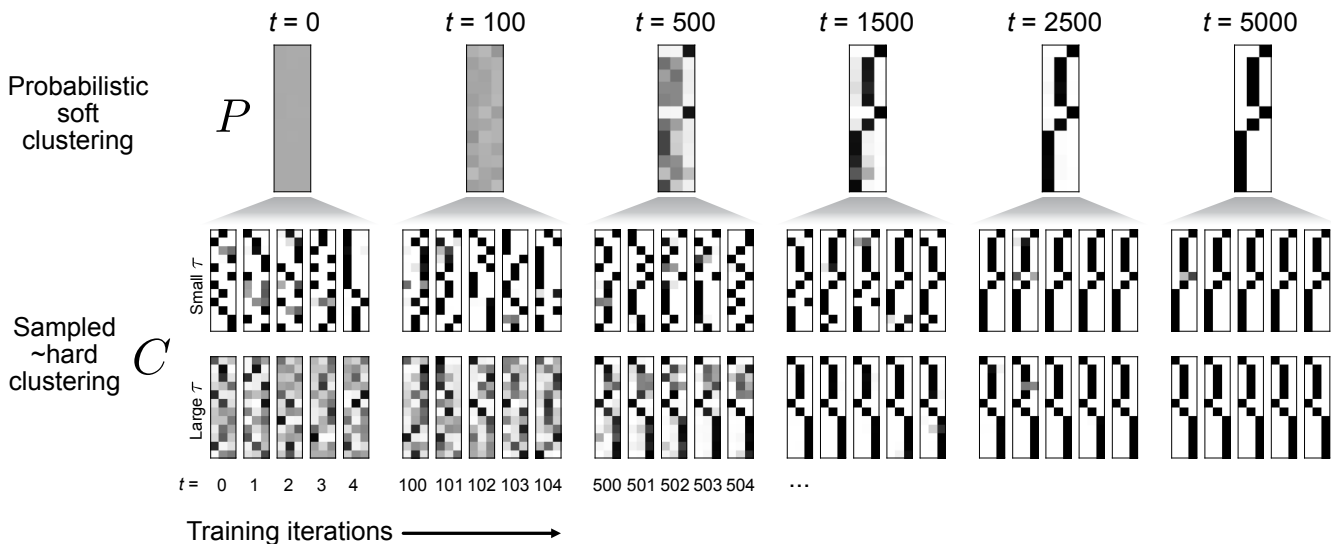


Supplementary Figure S1: Illustration of the Gumbel softmax trick for generating a clustering matrix The central matrix P denotes the probabilistic clustering matrix. It is derived (via softmax) from the matrix L to the left, the real-valued matrix of logits which are updated by gradient descent. Each row of P describes the probabilistic group assignment of a single species to different groups. From P , an approximately *hard* clustering matrix C is sampled using the Gumbel softmax trick described in Methods. Each row is approximately a one-hot vector that describes the group identity of the species.

Each row is the cluster assignment of a single species. The question is how to encode this matrix with continuous variables so that we may perform gradient descent.

This is achieved with the Gumbel softmax trick [52–54], a method for differentially sampling categorical variables. For us, the categorical variable is the cluster identity (e.g., a single entry in the vector \hat{c}). This sampling scheme will essentially allow us to “try” many different possible clusterings \hat{c} during training. To do this, each one-hot encoding of cluster identity (one row in C) is replaced by a soft assignment π of length N_{clust} . Instead of being a one-hot vector, π represents the *probability* of being assigned to each cluster. For example, $\pi = (0.08, 0.90, 0.02)$ says that there is an 8% chance of being clustered into group 1, a 90% chance of being clustered into group 2, etc. While we hope that this converges to a hard clustering during training so that each species is deterministically assigned to one group (i.e. probability of assignment becomes a delta function on group k : $\pi = (0, \dots, 1, \dots, 0)$), in practice this is not always the case. This represents real uncertainty about which group a species is assigned to. The distributions for all species are represented by a matrix $P \in [0, 1]^{n \times N_{\text{clust}}}$. Each row is distribution π_i for species i and sums to one.

While SCiFI is continuously adjusting P behind the scenes, we still ensure that the neural network only ever sees “hard” clusterings during training. To do this we sample a hard clustering C using the above matrix P : for every species (row), a group assignment (one hot vector) is generated



Supplementary Figure S2: Illustration of P and C matrices during training on a toy dataset. (Top) The probabilistic clustering P evolves slowly during training. (Bottom two rows) At each training step, an approximately hard clustering matrix C is sampled. For small τ (middle) this approximation is closer.

by sampled from the distribution in the corresponding row of P (bottom of Fig. S1). The Gumbel-softmax trick achieves this by randomly drawing a matrix $\Gamma \in \mathbb{R}^{n \times N_{\text{clust}}}$, where each entry is Gumbel distributed, and with it computing

$$C = \text{softmax} \left(\frac{1}{\tau} (\Gamma + \log P) \right) \quad (5)$$

where the softmax is taken over rows (i.e. each row is normalized to sum to 1) [52–54]. The matrix C is a sample of a hard clustering, consisting of approximately zeros and ones (the approximation is better as $\tau \rightarrow 0$). The relationship between C and P is shown for two different values of τ in Figs. S1 and S2. In particular, Figure S2 shows how, while P evolves slowly in time to the correct clustering, C undergoes large changes due to the stochastic sampling which enables SCiFI to explore many possible clusterings.

Step-by-step guide to training

Here we present a step-by-step guide that explains the full training procedure in detail.

Step 1: Data preparation. The data should consist of pairs $\{x_i, f_i\}$ where $x_i \in \mathbb{R}^n$ is a single (row) vector of abundances and $f_i \in \mathbb{R}^m$ is the corresponding vector of functional measurements. By assembling individual samples into a matrix we have $X \in \mathbb{R}^{N \times n}$ $F \in \mathbb{R}^{N \times m}$ where N is the number of samples in the dataset. In all of the examples in this work we perform cross validation by choosing N_{ens} (ens = “ensemble”) different test/train splits of the dataset. We typically choose $N_{\text{train}} = 0.8 \cdot N$ training samples with the remaining 20% used for testing. The 80% of samples used are randomly drawn from the dataset. We use an ensemble size of $N_{\text{ens}} = 12$ to 15. Let us write the set of training data for each ensemble member as $\{X_{\mu}^{\text{train}}, F_{\mu}^{\text{train}}\}$ where $\mu = 1..N_{\text{ens}}$, and analogously for the test data.

Step 2: SCiFI Training. We train one model per test/train split $\{X_{\mu}^{\text{train}}, F_{\mu}^{\text{train}}\}$, resulting in an ensemble of N_{ens} models. The neural network used here are small to mitigate overfitting, typically 3 layers with 128 neurons each. The precise width and depth do not strongly impact model

performance. The key hyperparameters which impact performance are the learning rate η and the “temperature” τ . We typically allow τ to reduce during training via an annealing schedule which decays exponentially from τ_{\max} (typically 1.0) to τ_{\min} (typically 0.1) at a rate r_τ . To determine the rate r_τ and the learning rate η we do a hyperparameter gridsearch over a handful of possible values for each. When gating is used, that introduces another hyperparameter β which is also included in this gridsearch. For a given set of hyperparameters we train the entire ensemble of models with their respective training data. Training is interrupted either due to the test loss ceasing to decrease (early stopping) or when a maximal number of iterations is reached.

Step 3: Post-processing and group extraction. The training procedure above generates an ensemble of N_{ens} clusterings. From this point on, we work with the soft clusterings $\{P_\mu\}_{\mu=1..N_{\text{ens}}}$. Due to stochasticity which arises both from the different training data splits and the Gumbel sampling trick, the matrices P_μ may show differences.

We extract a “consensus” clustering as follows. First, we sort the ensemble of models based on their predictive accuracy (R^2 of their function predictions versus the true predictions). Next, we choose a subset of high-performing models, typically the top 25% to 50%. In SI Fig. S15 we show how in the soil data, the consensus grouping is insensitive to the choice of how many top-performing models we take. We then make the consensus grouping based on majority rule: i.e. if five ensemble members assign species i to group 1 and four assign it to group 2, then the consensus assignment will be to group 1. When gating is used, the above procedure is modified slightly by adding the additional condition that species are only included in the consensus grouping if they are not gated in a majority of ensemble members. Clusterings are only unique up to a permutation invariance which we must account for. In other words, the groups $\{1, 2, 3\}$ for one model may correspond to the groups $\{2, 3, 1\}$ in another model just because of the arbitrariness of the group labeling. We correct for this by reordering groups based on their average abundance, or, in the case of the ocean metagenome, based on their correlation coefficient with nitrate.

Simulated data

To test SCiFI we construct a simulated dataset where community function arises as an effectively nonlinear combination of group abundances. Such an effective nonlinearity may come about even from a structure-function mapping with a linear form if the linear coefficients vary according to some hidden parameter. This is inspired by datasets which aggregate samples from environments which vary either naturally or due to experimentally-applied perturbations. For example, this may occur in communities which modulate their behavior depending on pH, which is directly relevant for the gut and soil datasets we consider later.

We consider a simulated dataset consisting of 3 groups assembled from 12 species. The function depends linearly on the group abundances,

$$f(x) = \sum_{i=1}^3 a_i G_i(x) = \sum_{i=1}^3 a_i \sum_{j \in I_i} x_j \quad (6)$$

where \vec{a} is a vector of parameters and I_i is the set of species indices that are in group i . To model the effect of varying environment (either due to perturbation or naturally-occurring), we let the parameter vector a vary across three “regimes”:

$$\vec{a}^{(1)} = (0.1, 1, 1), \quad \text{when } (G_1 > \text{med}(G_1)) \wedge (G_2 > \text{med}(G_2)) \quad (7)$$

$$\vec{a}^{(2)} = (1, -0.5, -0.1), \quad \text{when } (G_1 > \text{med}(G_1)) \wedge (G_2 < \text{med}(G_2)) \quad (8)$$

$$\vec{a}^{(3)} = (-1, 0.1, -1), \quad \text{when } (G_1 < \text{med}(G_1)) \quad (9)$$

where $\text{med}(G)$ denotes the median abundance of group G . Although the functional form of f is linear in Eq. (6), globally it is nonlinear due to the dependence of the parameters \vec{a} on regime.

Evaluation with Jaccard Index

Because the true groupings are known in this synthetic example, we can evaluate the quality of the group recovery using the Jaccard index. The Jaccard index compares the overlap (intersection) between two groupings with their union. To compare group i from one grouping with group j from another, one computes

$$J_{ij} = \frac{N_{\text{species in group } i \text{ AND group } j}}{(N_{\text{species in group } i}) + (N_{\text{species in group } j})}$$

If rows of J correspond to the ground truth groups, then the group recovery for group i is given by $J_i = \max_j J_{ij}$. The total Jaccard index is given as the average across all groups, $J = \frac{1}{G} \sum_{i=1}^G J_i$ where G denotes the number of groups.

Mathematical Modeling

For the mathematical modeling in Fig. 5 we start from the approach used in Ref. [36]. Our model (Eq. 2) is a minimal two-biomass extension of the single-biomass consumer resource model introduced in that work. The full dynamical system is given by

$$\dot{x}_1 = \gamma_1 r_1 x_1 \frac{A}{A + K_A} \frac{C}{C + K_C} \quad (10)$$

$$\dot{x}_2 = \gamma_2 r_2 x_2 \frac{A}{A + K_A} \frac{C}{C + K_C} \quad (11)$$

$$\dot{A} = -(r_1 x_1 + r_2 x_2) \frac{A}{A + K_A} \quad (12)$$

$$\dot{C} = -(x_1 + r_C x_2) \frac{C}{C + K_C}. \quad (13)$$

The carbon consumption equation starts from a similar form to that for nitrate A , but we absorbed the rate that multiples x_1 by rescaling C so that there is only one remaining parameter r_C . The full set of parameters to be determined are $\{\gamma_1, \gamma_2, r_1, r_2, r_C, C_0, K_A, K_C\}$, where C_0 is the initial carbon abundance; we treat the $\{\gamma_1, \gamma_2, K_A, K_C, r_C\}$ as parameters which are fixed across all conditions, while the rates $\{r_1, r_2, C_0\}$ may vary from sample to sample which reflects how reduction rates and carbon availability change with pH [36]. The goal is to optimize the parameters so that the above ordinary differential equation (ODE) correctly predicts the end-point biomasses and the evolution of nitrate concentration $\{x_1(T), x_2(T), A(t_1), \dots, A(T)\}$ starting from the (experimentally measured) initial conditions $\{x_1(0), x_2(0), A(0)\}$.

This is an instance of an ODE-constrained optimization problem. While the parameters may be found with e.g. the adjoint method, this approach is computationally slow. We instead rely on the fact that the dynamics is approximately given by an analytic solution. As long as the nutrients are not depleted ($A > 0$ and $C > 0$) the growth is approximately exponential, as is the depletion of A and C . When one of these is depleted, growth ceases so that $x_1 = \text{const}$, $x_2 = \text{const}$, and A decays linearly in time. In this procedure, we can use the analytical solution and search for the depletion time t^* instead of the initial carbon C_0 . The results are insensitive to the affinities K_A and K_C and so we fix them to some small value (10^{-3}). We find the remaining global parameters using a grid search over a range of possible hyperparameters, and find $\gamma_1 = 0.4$, $\gamma_2 = 2.44$ and results which are insensitive to $r_C = 1$. More information about this approach may be found in Ref. [36].

Null model comparison

To evaluate whether our groups are the “correct” variables in the mathematical model, we compare the performance of the fit model to the performance of one fit using randomized groupings. Random groups are generated as follows: For a particular group, say Group i , we construct an assembly of species whose total initial abundance is approximately equal to the initial abundance of Group i . We can randomize just a single group, or both groups, after which we apply the same fitting procedure as used for the consumer resource model in the main text. The result of this procedure is shown in SI Fig. S16.

We consider the randomization of both groups, only group 1, or only group 2; each case corresponds to one column in Fig. S16. Each panel shows the distribution of errors of the null model. Top row shows biomass 1 (mean squared) error, middle row shows biomass 2 error, and bottom row shows the error in nitrate prediction. Each plot highlights with a black outline the distribution that arises from shuffling the variable denoted in that column; the distributions from the other randomization procedures are not highlighted but shown in all panels for comparison. We compare the highlighted distributions to the model error using the “correct” groups (shown as vertical dashed line) by computing the p -value shown in the upper right corner.

We find that shuffling either of the biomasses individually or both together leads to significantly worse performance than the true model (bottom row). However, shuffling biomass 2 only, while still worse than the true model, degrades performance to a lesser extent than the other two randomization procedures (horizontal arrow in bottom row). There is also almost no effect on the prediction of biomass 1 (arrow in top row). Shuffling biomass 1 significantly degrades predictive power for both nitrate dynamics and biomass 1 end-point abundance. However, the performance in biomass 2 prediction actually increases (arrow in middle row), possibly hinting that it could not be as accurately predicted because of a trade-off in the model’s ability to predict both biomass 1 and biomass 2. Together, these results suggest that biomass 2 is not as important as biomass 1 in making predictions of nitrate dynamics or biomass 1 dynamics.

Microbiome datasets

Human gut synthetic community dataset

Synthetic community experiments with human gut microbial strains were done by Clark *et al.* (2021), where they inoculated 1850 different combinations of 26 representative gut strains in the media in the anaerobic chamber to measure the final concentrations of produced butyrate, succinate, acetate, and lactate. For each synthetic community, the relative abundance of the endpoint community was measured by 16S rRNA amplicon sequencing as described by the original authors [32]. We used the endpoint relative abundance of strains as compositional input and produced butyrate and succinate concentrations as functional output for training the neural network. The gene annotation information of each strain’s genome (Biocyc database) from the original authors [33] was used to validate the functional clusters by enzyme presence or absence. The dimension (sample \times strain) of the compositional data was 1850×26 . The functional data used for neural network prediction had a dimension (sample \times metabolite concentration) of 1850×1 , respectively for butyrate and succinate.

Tara Oceans natural community dataset

136 Tara Oceans samples were sampled by the original authors [34, 35] across the oceans at different depths. For each sample, they measured nitrate concentration, temperature, and dissolved oxygen level (6 samples have NaN values for at least one of these measurements and are omitted), which we used as functional outputs to train the neural network. The relative abundance of taxa in each sample was derived from 16S rDNA fragments in the metagenomic sequencing (miTAGs) as

described by the original authors [34, 35] and Shan et al [24]. The dimension (sample \times taxa) of the compositional data was 136 \times 97 at the genus level.

For the gene module abundance of each sample, we used the annotated gene tables uploaded by the original authors [34, 35]. The dimension (sample \times gene) of the gene composition data was 136 \times 515 for module-level annotation. The functional data used for neural network prediction had a dimension (sample \times environmental variable) of 136 \times 1 for the case we identify functional groupings with nitrate concentrations or 130 \times 3 for the case we use all 3 environmental variables (nitrate concentration, temperature, and dissolved oxygen level) to identify functional groups, as we removed 6 samples without corresponding oxygen measurements.

Soil pH perturbation dataset

20 Topsoils were collected across a native pH gradient (4.7–8.32) in the Cook Agronomy Farm (CAF) in the Long-Term Agroecosystem Research (LTAR) (Pullman, WA, USA) and perturbed each soil slurry into 13 different pH levels as well as adding 2mM nitrate to initiate denitrification in 1:2 soil-to-water slurries under anaerobic conditions, as described previously. [36]. To infer indigenous biomass activity of nitrate reduction, we included chloramphenicol-treated (CHL+) controls, in which protein synthesis and growth were inhibited, yielding linear nitrate reduction dynamics. In contrast, untreated controls (CHL-) allowed microbial growth and physiological responses to the imposed pH conditions. For functional outputs, we measured the functional dynamics (10 time points during the 4-day incubation) of nitrate, nitrite, and ammonium concentrations. The absolute abundance of each taxon per sample was acquired by dividing reads from 16S rRNA amplicon sequencing with reads from the internal standard of known spiked-in strains [36]. 16S rRNA amplicon sequencing was performed on endpoint perturbed samples derived from 10 of the 20 CAF sampled soils.

We removed 18 samples lacking complete triplicate CHL+/CHL- pairs in Soil12 (perturbed unit 20 and 40) and Soil15 (perturbed unit 12). We removed taxa that had fewer than 1,000 total reads across the entire sequencing dataset to minimize noise and sparsity coming from very low-abundance taxa. The dimensions (sample \times taxa) of the compositional data were 762 \times 28 for phyla, 762 \times 256 for family, and 762 \times 4395 for ASV level. The functional data used for neural network prediction had a dimension (sample \times metabolite dynamics) of 762 \times 10 for nitrate, 762 \times 20 for nitrate and nitrite, 762 \times 30 for nitrate, nitrite, and ammonium.

Strain isolation and whole genome sequencing

For isolation, as described previously [36], we thawed endpoint slurry samples from soil pH perturbation experiments stored in 25% glycerol in -80°C, streaked onto 1/10 \times tryptic soy agar (TSA) plates and 1/10 \times Reasoner’s 2A (R2A) plates adjusted to the endpoint pH of each slurry sample. Plates were incubated at 30°C and checked for growth every 24 hours. Genomic DNA was extracted from pure colonies using the DNeasy Ultraclean Microbial Kit (Qiagen, Hilden, Germany). Unique strains were identified by Sanger sequencing of the 16S rRNA region amplified by 27F and 1492R primers, followed by BLAST against the NCBI 16S rRNA reference sequences for taxonomic identification. We decided to further investigate the genetic composition of the two strains taxonomically identified as *Neobacillus fumarioli* (Group 1 representative strain) and *Peribacillus simplex* (Group 2 representative strain) with whole genome sequencing.

For whole-genome sequencing, approximately 5×10^9 cells were preserved in DNA/RNA Shield (Zymo Research) and submitted to Plasmidsaurus (USA). Genomic DNA was prepared using an amplification-free library construction protocol (ONT V14 chemistry) and sequenced on Oxford Nanopore Technology (ONT) R10.4.1 flow cells. Raw signals were basecalled using the Dorado

Super-Accurate (SUP) model with a default Q10 quality filter. Read quality was further refined by removing the lowest 5% of reads using Filtlong v0.2.1. De novo assembly was executed via the Autocycler pipeline, which generates a consensus from multiple independent assemblers, including Flye v2.9.6+, Hifiasm, and Plasmemblem v1.8.0+. The final consensus assembly was polished using Medaka v1.8.0 and oriented to the dnaA start position using dnaapl. Structural and functional annotation was performed using Bakta v1.11.4 utilizing the v6.0 full database. Species identification was verified through Mash v2.3 and Sourmash v4.6.1 against RefSeq and GenBank databases, while genome completeness and contamination were assessed via CheckM v1.2.2.

Dataset	Input	Function	N_{samples}	N_{train}	N_{ens}	Figure
Gut (synth.) [32]	Strains ($d = 30$)	Butyrate ($d = 1$)	1592	1273	20	3a-d
Gut (synth.) [32]	Strains ($d = 30$)	Succinate ($d = 1$)	1592	1273	20	3e-h
Ocean [34]	Genera ($d = 97$)	NO_3 ($d = 1$)	136	108	15	3i-l
Soil [36]	Phyla ($d = 28$)	$\text{NO}_3(\text{t})$ ($d = 10$)	381	304	15	3m-p
Ocean [34]	Gene modules ($d = 515$)	$(\text{NO}_3, \text{O}_2, \text{T})$ ($d = 3$)	130	104	12	4
Soil [36]	ASVs ($d = 4395$)	$\text{NO}_3(\text{t})$ ($d = 10$)	762	570	12	5,6

Table 1: Dataset overview Summary of each dataset used in this work. Input states how abundance data is defined, with d the dimension (number of species/genes). Function states the functional data and its dimensionality d . The total number of samples in the dataset is given by N_{samples} , and the number of samples used for training is N_{train} . The number of samples in the two rows of the ocean dataset differ because some values of oxygen concentration are missing, which means we omit these samples. The number of samples differs between the two soil datasets because in the first case only non-treated samples are used, while in the second both chloramphenicol-treated and non-treated samples are used. The number of models trained in the whole ensemble is given by N_{ens} ; for details see the “Step-by-step guide to training” in Methods.

Data availability

All data used to train the neural networks will be made available upon publication.

Code availability

Code deploying our method on a synthetic dataset may be found in github.com/schmittms/function_informed_clustering. All code used to generate the figures will be made public upon acceptance for publication.

ACKNOWLEDGEMENTS

The soil-related research was conducted as part of the Long-Term Agroecosystem Research (LTAR) Network, which is supported by the United States Department of Agriculture. We thank Otto Cordero for constructive discussions and feedback. We acknowledge Jocelyn Wang for soil strain isolation.

This research was supported in part by grants from the NSF (DMS-2235451) and Simons Foundation (MPS-NITMB-00005320) to the NSF-Simons National Institute for Theory and Mathematics in Biology (NITMB). S.K. acknowledges the Center for the Physics of Evolving Systems at the University of Chicago, National Institute of General Medical Sciences R01GM151538. S.K. acknowledges a CAREER award from the National Science Foundation (BIO/MCB 2340416). V.V. and S.K. acknowledge support from the National Science Foundation through the Physics Frontier Center for Living Systems (PHY2317138). V. V. is a Chan Zuckerberg Biohub Chicago Investigators. Any opinions, findings, conclusions, or recommendations expressed in this material are those

of the authors and do not necessarily reflect the views of the National Science Foundation. S.K. acknowledges support from the Army Research Office (AWD106455). This work was completed in part with resources provided by the University of Chicago’s Research Computing Center.

REFERENCES

- [1] Yinon M. Bar-On, Rob Phillips, and Ron Milo. The biomass distribution on earth. *Proceedings of the National Academy of Sciences*, 115(25):6506–6511, 2018.
- [2] D. L. Warner, B. Bond-Lamberty, J. Jian, E. Stell, and R. Vargas. Spatial Predictions and Associated Uncertainty of Annual Soil Respiration at the Global Scale. *Global Biogeochemical Cycles*, 33(12):1733–1745, December 2019.
- [3] Ben Bond-Lamberty, Vanessa L. Bailey, Min Chen, Christopher M. Gough, and Rodrigo Vargas. Globally rising soil heterotrophic respiration over recent decades. *Nature*, 560(7716):80–83, August 2018.
- [4] Shoji Hashimoto, Akihiko Ito, and Kazuya Nishina. Divergent data-driven estimates of global soil respiration. *Communications Earth & Environment*, 4(1):460, December 2023.
- [5] Marcel M. M. Kuypers, Hannah K. Marchant, and Boran Kartal. The microbial nitrogen-cycling network. *Nature Reviews Microbiology*, 16(5):263–276, May 2018.
- [6] KA Third, A Olav Sliemers, JG Kuenen, and MSM Jetten. The canon system (completely autotrophic nitrogen-removal over nitrite) under ammonium limitation: interaction and competition between three groups of bacteria. *Systematic and applied microbiology*, 24(4):588–596, 2001.
- [7] Frances Spragge, Erik Bakkeren, Martin T. Jahn, Elizete B. N. Araujo, Claire F. Pearson, Xuedan Wang, Louise Pankhurst, Olivier Cunrath, and Kevin R. Foster. Microbiome diversity protects against pathogens by nutrient blocking. *Science*, 382(6676):eadj3502, December 2023.
- [8] Sergius Winogradsky. Über Schwefelbakterien. *Botanische Zeitung*, 45(31):489–512, 1887.
- [9] Harry J. Flint. The rumen microbial ecosystem—some recent developments. *Trends in Microbiology*, 5(12):483–488, December 1997.
- [10] Tim N. Enke, Manoshi S. Datta, Julia Schwartzman, Nathan Cermak, Désirée Schmitz, Julien Barrere, Alberto Pascual-García, and Otto X. Cordero. Modular Assembly of Polysaccharide-Degrading Marine Microbial Communities. *Current Biology*, 29(9):1528–1535.e6, May 2019.
- [11] M.T. Madigan, J.M. Martinko, K.S. Bender, D.H. Buckley, and D.A. Stahl. *Brock Biology of Microorganisms*. Always learning. Pearson, 2014.
- [12] Marc Strous, John A. Fuerst, Evelien H. M. Kramer, Susanne Logemann, Gerard Muyzer, Katinka T. van de Pas-Schoonen, Richard Webb, J. Gijs Kuenen, and Mike S. M. Jetten. Missing lithotroph identified as new planctomycete. *Nature*, 400(6743):446–449, Jul 1999.
- [13] Douglas E. Rawlings. Heavy Metal Mining Using Microbes. *Annual Review of Microbiology*, 56(1):65–91, October 2002.

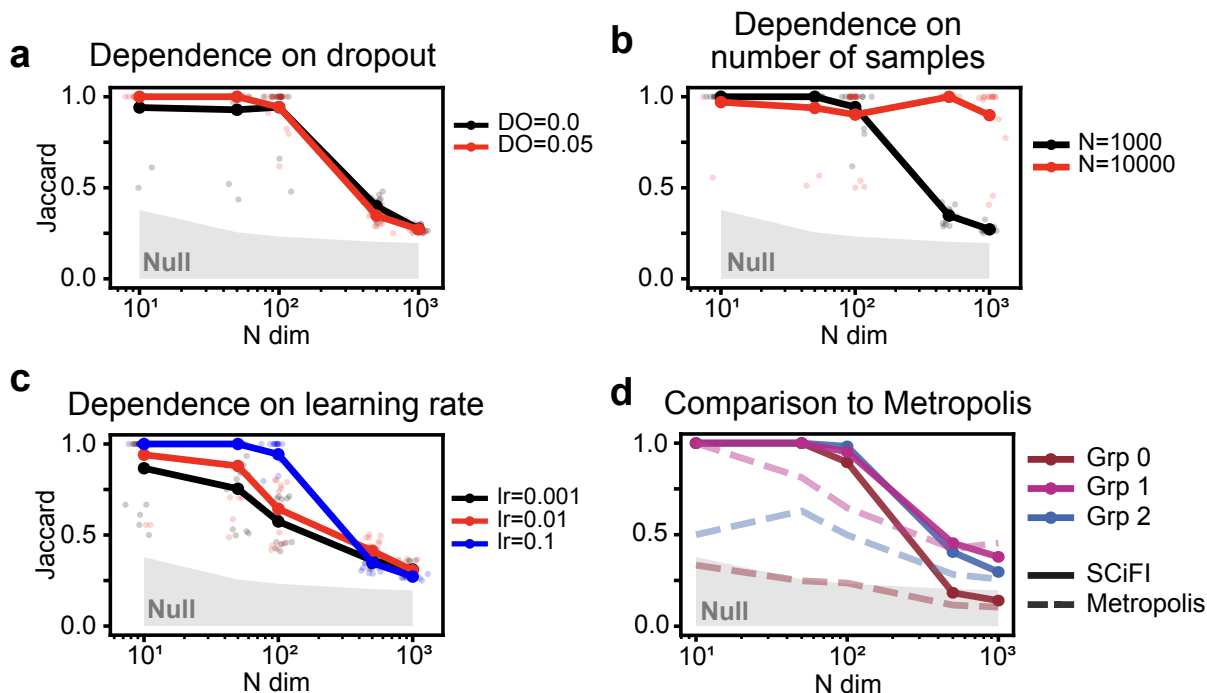
- [14] M. P. Bryant, E. A. Wolin, M. J. Wolin, and R. S. Wolfe. Methanobacillus omelianskii, a symbiotic association of two species of bacteria. *Archiv für Mikrobiologie*, 59(1-3):20–31, 1967.
- [15] Holger Daims, Elena V. Lebedeva, Petra Pjevac, Ping Han, Craig Herbold, Mads Albertsen, Nico Jehmlich, Marton Palatinszky, Julia Vierheilig, Alexandr Bulaev, Rasmus H. Kirkegaard, Martin Von Bergen, Thomas Rattei, Bernd Bendinger, Per H. Nielsen, and Michael Wagner. Complete nitrification by Nitrospira bacteria. *Nature*, 528(7583):504–509, December 2015.
- [16] Mary K. Firestone and James M. Tiedje. Temporal Change in Nitrous Oxide and Dinitrogen from Denitrification Following Onset of Anaerobiosis. *Applied and Environmental Microbiology*, 38(4):673–679, October 1979.
- [17] J. M. Bremner and A. M. Blackmer. Nitrous Oxide: Emission from Soils During Nitrification of Fertilizer Nitrogen. *Science*, 199(4326):295–296, January 1978.
- [18] Grace Pold, Aurélien Saghai, Christopher M. Jones, and Sara Hallin. Denitrification is a community trait with partial pathways dominating across microbial genomes and biomes. *Nature Communications*, 16(1):9495, October 2025.
- [19] Thomas N. Gamble, Michael R. Betlach, and James M. Tiedje. Numerically Dominant Denitrifying Bacteria from World Soils. *Applied and Environmental Microbiology*, 33(4):926–939, April 1977.
- [20] Kyle Crocker, Kiseok Keith Lee, Milena Chakraverti-Wuerthwein, Zeqian Li, Mikhail Tikhonov, Madhav Mani, Karna Gowda, and Seppe Kuehn. Environmentally dependent interactions shape patterns in gene content across natural microbiomes. *Nat. Microbiol.*, pages 1–16, 2024.
- [21] Najeeb Halabi, Olivier Rivoire, Stanislas Leibler, and Rama Ranganathan. Protein Sectors: Evolutionary Units of Three-Dimensional Structure. *Cell*, 138(4):774–786, August 2009.
- [22] Thomas Vierbuchen, Austin Ostermeier, Zhiping P. Pang, Yuko Kokubu, Thomas C. Südhof, and Marius Wernig. Direct conversion of fibroblasts to functional neurons by defined factors. *Nature*, 463(7284):1035–1041, February 2010.
- [23] W J Jones, D P Nagle, and W B Whitman. Methanogens and the diversity of archaebacteria. *Microbiological Reviews*, 51(1):135–177, March 1987.
- [24] Xiaoyu Shan, Akshit Goyal, Rachel Gregor, and Otto X. Cordero. Annotation-free discovery of functional groups in microbial communities. *Nature Ecology & Evolution*, 7(5):716–724, May 2023.
- [25] Yuanchen Zhao, Otto X. Cordero, and Mikhail Tikhonov. Linear-regression-based algorithms can succeed at identifying microbial functional groups despite the nonlinearity of ecological function. *PLOS Computational Biology*, 20(11):e1012590, November 2024.
- [26] Karoline Faust, J. Fah Sathirapongsasuti, Jacques Izard, Nicola Segata, Dirk Gevers, Jeroen Raes, and Curtis Huttenhower. Microbial Co-occurrence Relationships in the Human Microbiome. *PLoS Computational Biology*, 8(7):e1002606, July 2012.
- [27] Zachary D. Kurtz, Christian L. Müller, Emily R. Miraldi, Dan R. Littman, Martin J. Blaser, and Richard A. Bonneau. Sparse and Compositionally Robust Inference of Microbial Ecological Networks. *PLOS Computational Biology*, 11(5):e1004226, May 2015.

- [28] Jonathan Friedman and Eric J. Alm. Inferring correlation networks from genomic survey data. *PLoS computational biology*, 8(9), 2012.
- [29] Dirk Gevers, Subra Kugathasan, Lee A. Denson, Yoshiki Vázquez-Baeza, Will Van Treuren, Boyu Ren, Emma Schwager, Dan Knights, Se Jin Song, Moran Yassour, Xochitl C. Morgan, Aleksandar D. Kostic, Chengwei Luo, Antonio González, Daniel McDonald, Yael Haberman, Thomas Walters, Susan Baker, Joel Rosh, Michael Stephens, Melvin Heyman, James Markowitz, Robert Baldassano, Anne Griffiths, Francisco Sylvester, David Mack, Sandra Kim, Wallace Crandall, Jeffrey Hyams, Curtis Huttenhower, Rob Knight, and Ramnik J. Xavier. The Treatment-Naive Microbiome in New-Onset Crohn’s Disease. *Cell Host & Microbe*, 15(3):382–392, March 2014.
- [30] Ina Maria Deutschmann, Gipsi Lima-Mendez, Anders K. Krabberød, Jeroen Raes, Sergio M. Vallina, Karoline Faust, and Ramiro Logares. Disentangling environmental effects in microbial association networks. *Microbiome*, 9(1):232, December 2021.
- [31] Xiaoyuan Zhou, Ryan Baumann, Xiaohui Gao, Myra Mendoza, Sneha Singh, Ilana Katz Sand, Zongqi Xia, Laura M. Cox, Tanuja Chitnis, Hongsup Yoon, Laura Moles, Stacy J. Caillier, Adam Santaniello, Gail Ackermann, Adil Harroud, Robin Lincoln, Refujia Gomez, Antonio González Peña, Elise Digga, Daniel Joseph Hakim, Yoshiki Vazquez-Baeza, Karthik Soman, Shannon Warto, Greg Humphrey, Mauricio Farez, Lisa Ann Gerdes, Jorge R. Oksenberg, Scott S. Zamvil, Siddharthan Chandran, Peter Connick, David Otaegui, Tamara Castillo-Triviño, Stephen L. Hauser, Jeffrey M. Gelfand, Howard L. Weiner, Reinhard Hohlfeld, Hartmut Wekerle, Jennifer Graves, Amit Bar-Or, Bruce A.C. Cree, Jorge Correale, Rob Knight, and Sergio E. Baranzini. Gut microbiome of multiple sclerosis patients and paired household healthy controls reveal associations with disease risk and course. *Cell*, 185(19):3467–3486.e16, September 2022.
- [32] Ryan L. Clark, Bryce M. Connors, David M. Stevenson, Susan E. Hromada, Joshua J. Hamilton, Daniel Amador-Noguez, and Ophelia S. Venturelli. Design of synthetic human gut microbiome assembly and butyrate production. *Nat. Commun.*, 12(1):3254, 2021.
- [33] Yili Qian, Sarvesh D. Menon, Nick Quinn-Bohmann, Sean M. Gibbons, and Ophelia S. Venturelli. A data-driven modeling framework for mapping genotypes to synthetic microbial community functions. *bioRxiv*, 2025.
- [34] Shinichi Sunagawa, Luis Pedro Coelho, Samuel Chaffron, Jens Roat Kultima, Karine Labadie, Guillem Salazar, Bardya Djahanschiri, Georg Zeller, Daniel R Mende, Adriana Alberti, et al. Structure and function of the global ocean microbiome. *Science*, 348(6237):1261359, 2015.
- [35] Stilianos Louca, Laura Wegener Parfrey, and Michael Doebeli. Decoupling function and taxonomy in the global ocean microbiome. *Science*, 353(6305):1272–1277, 2016.
- [36] Kiseok Keith Lee, Siqi Liu, Kyle Crocker, Jocelyn Wang, David R. Huggins, Mikhail Tikhonov, Madhav Mani, and Seppe Kuehn. Functional regimes define soil microbiome response to environmental change. *Nature*, 644(8078):1028–1038, August 2025.
- [37] Minoru Kanehisa and Susumu Goto. Kegg: Kyoto encyclopedia of genes and genomes. *Nucleic Acids Research*, 28(1):27–30, 01 2000.

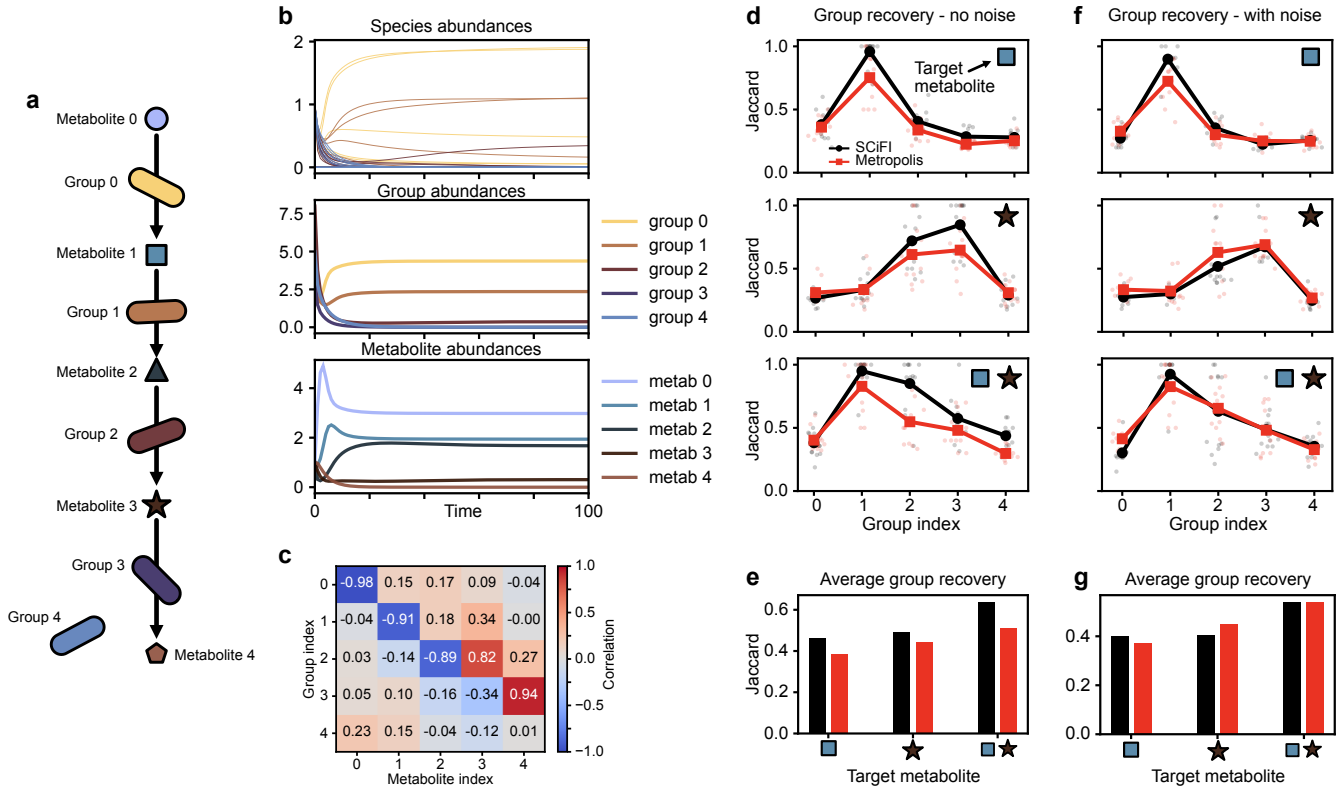
- [38] Minoru Kanehisa, Miho Furumichi, Yoko Sato, Yuriko Matsuura, and Mari Ishiguro-Watanabe. KEGG: biological systems database as a model of the real world. *Nucleic Acids Research*, 53(D1):D672–D677, January 2025.
- [39] Alan W. Decho. Microbial exopolymer secretions in ocean environments: their role(s) in food webs and marine processes. *Oceanography and Marine Biology: An Annual Review*, 28:73–153, 1990.
- [40] Alan W. Decho and Tony Gutierrez. Microbial Extracellular Polymeric Substances (EPSs) in Ocean Systems. *Frontiers in Microbiology*, 8:922, May 2017.
- [41] Gerhard J Herndl. Major role of ultraviolet-8 in controlling bacterioplankton growth in the surface layer of the ocean. *Nature*, 361, 1993.
- [42] MM Doolittle, JJ Cooney, and DE Caldwell. Lytic infection of escherichia coli biofilms by bacteriophage t4. *Canadian journal of microbiology*, 41(1):12–18, 1995.
- [43] Mohammad Bahram, Falk Hildebrand, Sofia K. Forslund, Jennifer L. Anderson, Nadejda A. Soudzilovskaia, Peter M. Bodegom, Johan Bengtsson-Palme, Sten Anslan, Luis Pedro Coelho, Helery Harend, Jaime Huerta-Cepas, Marnix H. Medema, Mia R. Maltz, Sunil Mundra, Pål Axel Olsson, Mari Pent, Sergei Pölme, Shinichi Sunagawa, Martin Ryberg, Leho Tedersoo, and Peer Bork. Structure and function of the global topsoil microbiome. *Nature*, 560(7717):233–237, August 2018.
- [44] Gavin M. Douglas, Vincent J. Maffei, Jesse R. Zaneveld, Svetlana N. Yurgel, James R. Brown, Christopher M. Taylor, Curtis Huttenhower, and Morgan G. I. Langille. PICRUSt2 for prediction of metagenome functions. *Nature Biotechnology*, 38(6):685–688, June 2020.
- [45] Karna Gowda, Derek Ping, Madhav Mani, and Seppe Kuehn. Genomic structure predicts metabolite dynamics in microbial communities. *Cell*, 185(3):530–546.e25, February 2022.
- [46] Felix Goldschmidt, Roland R Regoes, and David R Johnson. Metabolite toxicity slows local diversity loss during expansion of a microbial cross-feeding community. *The ISME Journal*, 12(1):136–144, January 2018.
- [47] Steven L. Brunton, Joshua L. Proctor, and J. Nathan Kutz. Discovering governing equations from data by sparse identification of nonlinear dynamical systems. *Proceedings of the National Academy of Sciences*, 113(15):3932–3937, April 2016.
- [48] Ricky T. Q. Chen, Yulia Rubanova, Jesse Bettencourt, and David K Duvenaud. Neural ordinary differential equations. In S. Bengio, H. Wallach, H. Larochelle, K. Grauman, N. Cesa-Bianchi, and R. Garnett, editors, *Advances in Neural Information Processing Systems*, volume 31. Curran Associates, Inc., 2018.
- [49] Juan A. Gallego, Matthew G. Perich, Lee E. Miller, and Sara A. Solla. Neural Manifolds for the Control of Movement. *Neuron*, 94(5):978–984, June 2017.
- [50] Apostolos P. Georgopoulos, Andrew B. Schwartz, and Ronald E. Kettner. Neuronal Population Coding of Movement Direction. *Science*, 233(4771):1416–1419, September 1986.

- [51] Veit R. Buchholz, Michael Flossdorf, Inge Hensel, Lorenz Kretschmer, Bianca Weissbrich, Patricia Gräf, Admar Verschoor, Matthias Schiemann, Thomas Höfer, and Dirk H. Busch. Disparate Individual Fates Compose Robust CD8⁺ T Cell Immunity. *Science*, 340(6132):630–635, May 2013.
- [52] Chris J. Maddison, Daniel Tarlow, and Tom Minka. A* sampling. In Z. Ghahramani, M. Welling, C. Cortes, N. Lawrence, and K.Q. Weinberger, editors, *Advances in Neural Information Processing Systems*, volume 27. Curran Associates, Inc., 2014.
- [53] Chris J. Maddison, Andriy Mnih, and Yee Whye Teh. The concrete distribution: A continuous relaxation of discrete random variables, 2017.
- [54] Eric Jang, Shixiang Gu, and Ben Poole. Categorical reparameterization with gumbel-softmax, 2017.
- [55] Glen Wheeler, Takahiro Ishikawa, Varissa Pornsaksit, and Nicholas Smirnoff. Evolution of alternative biosynthetic pathways for vitamin C following plastid acquisition in photosynthetic eukaryotes. *eLife*, 4:e06369, March 2015.
- [56] Rod G. Zika and William J. Cooper, editors. *Photochemistry of Environmental Aquatic Systems*, volume 327 of *ACS Symposium Series*. American Chemical Society, Washington, DC, December 1987.

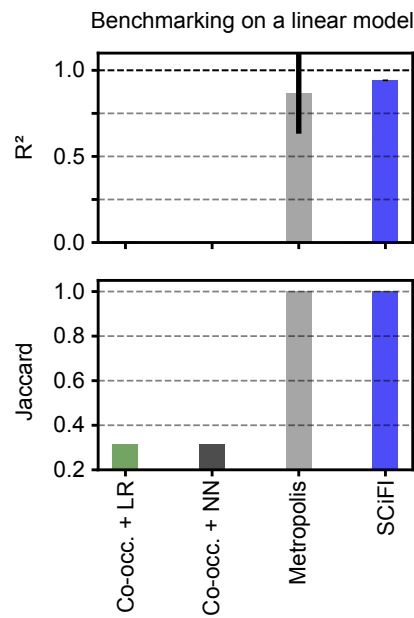
SUPPLEMENTARY INFORMATION



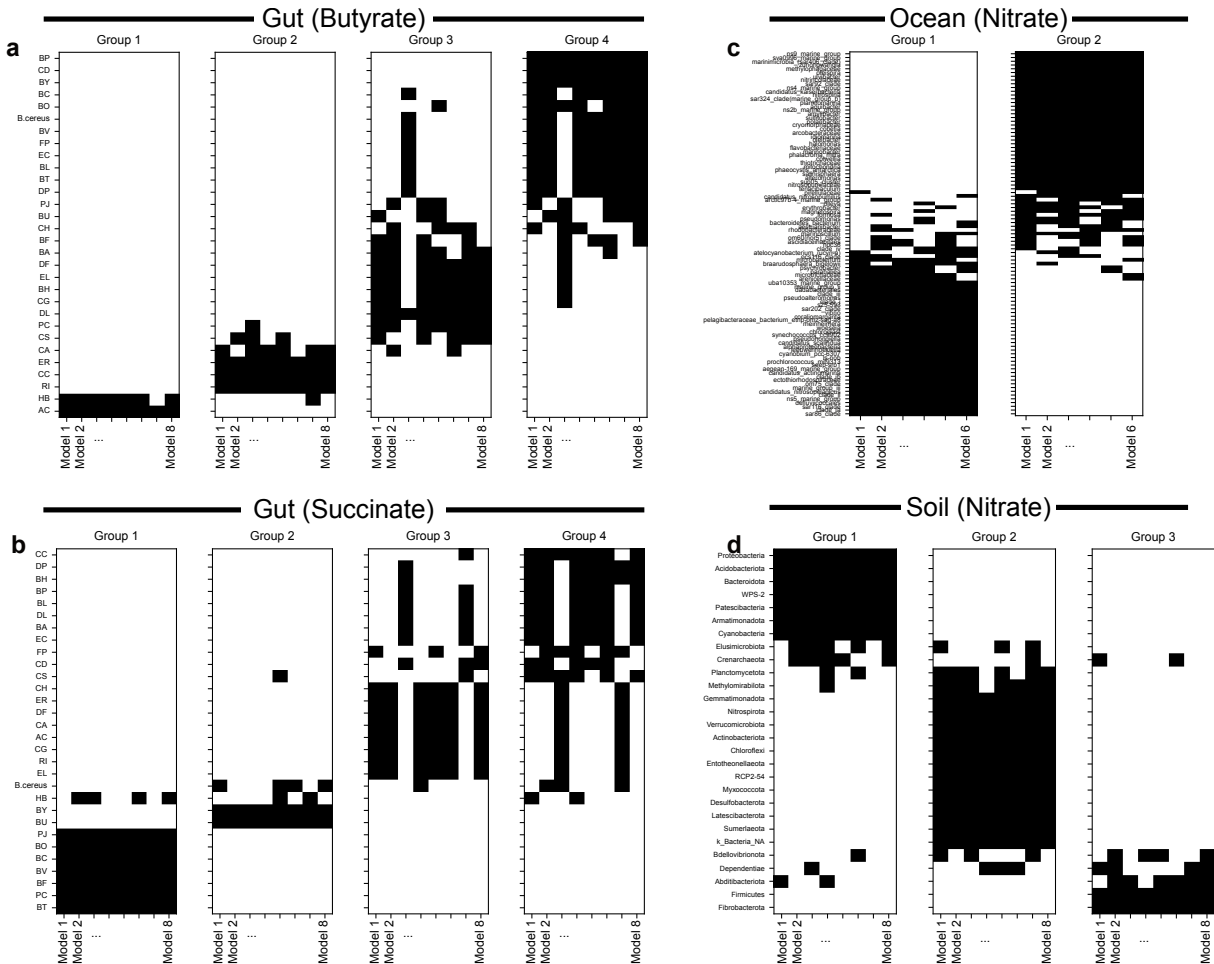
Supplementary Figure S3: Training hyperparameters impacting performance on synthetic data. We explore how SCiFI’s ability to recover the correct groups depends on critical training parameters and on the dimension of the input. The synthetic data follows the structure discussed in Methods and used in Fig. 2. The basic group structure is $\hat{c} = (1, 2, 2, 2, 3, 3, 3, 3, 3, 3)$ which assigns 10 species to 3 clusters. We vary the dimensionality of the system while keeping the group number fixed by simply repeating \hat{c} for an integer number of repetitions (e.g. 10 repetitions would correspond to a dimensionality of 100). The neural network used to model the structure function map is small, consisting of 2 layers of 48 neurons each. This small network is sufficient because the function is piecewise linear. In all cases we measure group recovery with the Jaccard index (see Methods). (a) Variation of group recovery as a function of dimensionality for different values of dropout. Every faint dot corresponds to one model of an ensemble ($N_{\text{ens}} = 15$), slightly jiggled in the x -direction for visualization. The solid dots with connecting line are the average Jaccard index across all ensemble members. The number of samples used for training is 1000 and we see performance start to decrease at $N_{\text{dim}} = 100$. Dropout makes negligible difference to the group recovery, but it significantly improves generalization (not shown). (b) Same as in (a) but varying the number of training samples. Performance increases significantly when the number of samples is increased. This suggests that given enough data, SCiFI should find the correct groups. (c) Same as in (c) but varying the learning rate during training. In general, learning rate can significantly impact performance. Here we see that using a larger learning rate improves group recovery. However, too large and the networks will fail to train (not shown). (d) Comparison of SCiFI group recovery to the Metropolis Hastings algorithm from Ref. [25]. Here we show the recovery of each group individually. SCiFI generically outperforms the Metropolis Hastings algorithm. Here we also see that the group recovery differs across groups. This suggests that the decrease in performance at $N_{\text{dim}} \approx 100$ is due to the particular structure-function map used.



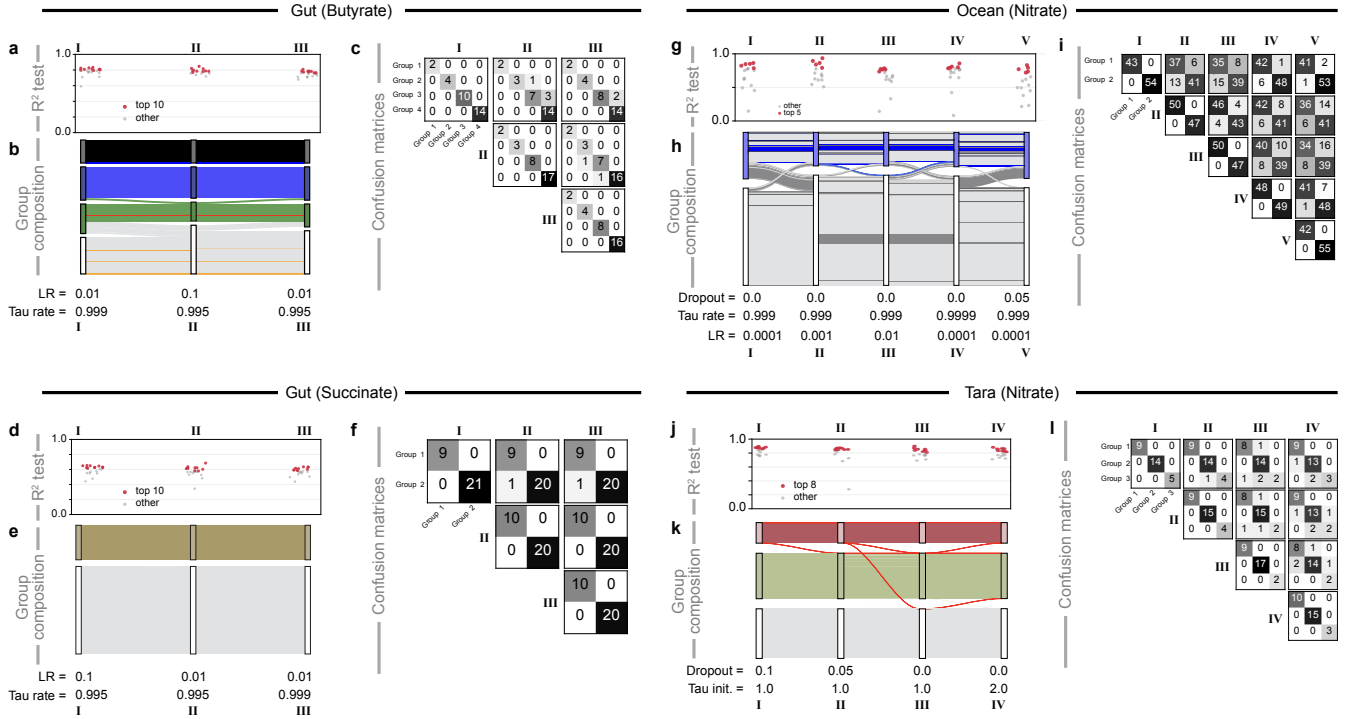
Supplementary Figure S4: SCiFI applied to a linear degradation chain. (a) Here we evaluate SCiFI on a simulated community of species which participate in a linear degradation chain of a metabolite as in Ref. [25]. The first four groups participate in the chain, the last group does not. (b) Evolution in time of the species abundances (top), grouped abundances (middle) and metabolite abundances (bottom). (c) Correlations between end-point group abundances and metabolite abundances. (d) Group recovery as measured by the Jaccard index for each group. Red shows the results of the Metropolis-Hastings algorithm from Ref. [25], black shows SCiFI. The icon in the upper right indicates what function (metabolite abundance) was used to train SCiFI. The top row uses metabolite 1, middle uses metabolite 3, and bottom uses both. (e) Average group recovery across all groups, separated by target metabolite algorithm (SCiFI - black, Metropolis - red). Group recovery improves when using multiple intermediate metabolites (right columns). (f-g) Same as in (d-e) but with added 10% noise on the metabolites concentrations. We see that the performance gap between SCiFI and Metropolis decreases. This is unsurprising because Ref. [25] shows that the Metropolis algorithm works well in this setting.



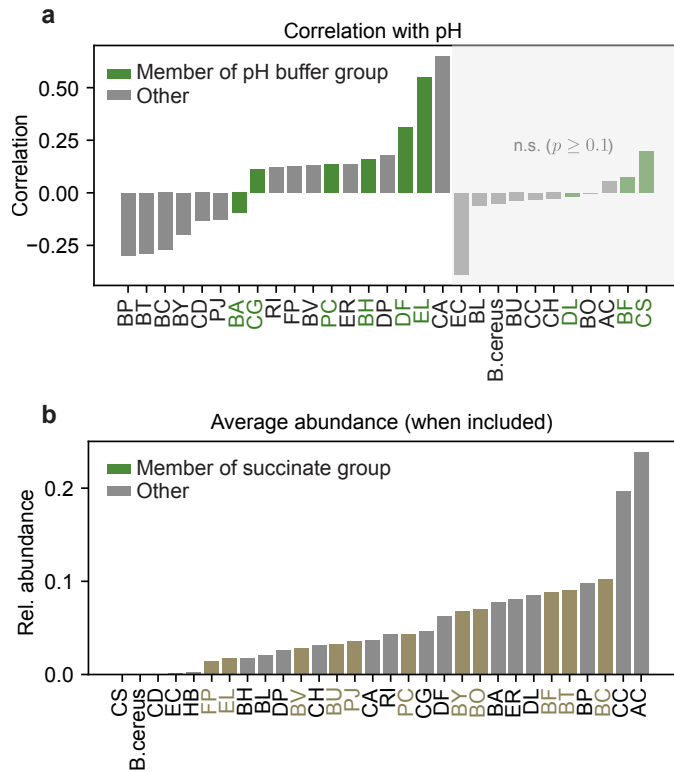
Supplementary Figure S5: Benchmarking on a linear model. This plot compares the same models as in Fig. 2d-e, but when the true structure-function map is linear. In this case we see that Model III (the Metropolis-Hastings algorithm from Ref. [25]) recovers the groups correctly. The co-occurrence models perform poorly because in this simulation there is no built-in correlation structure among different species.



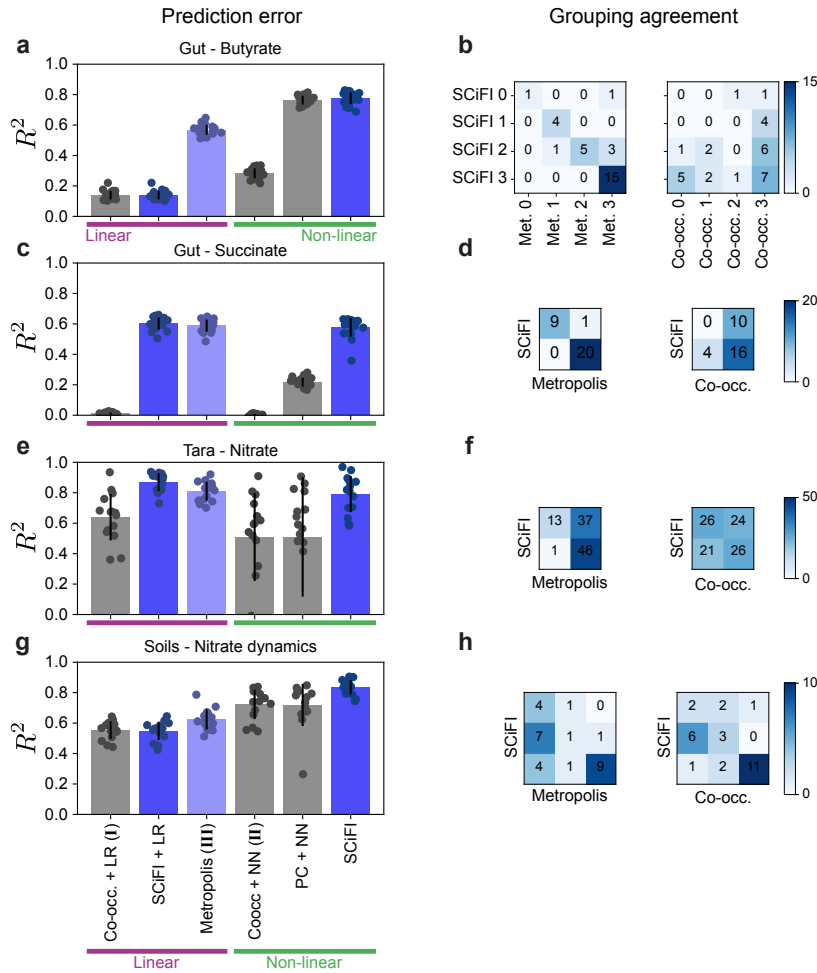
Supplementary Figure S6: Consistency of groups across test-train splits. For each of the datasets in Fig. 3 we illustrate the consistency of the learned groups across the different test/train splits used for cross validation. As a reminder, we train an ensemble of models with different test train splits (Methods). (a) Each matrix (left to right) corresponds to one group. Each column of the matrices in this figure corresponds to one model. Each row corresponds to one species. Black means the species is included in the corresponding group, white means it is not. For example, AC is always in Group 1, and CC is always in Group 2. Because the indices of the groups are arbitrary, we must reorder them so they are consistent across models. We do this by ordering the groups by their correlation with the target function. This process is imperfect as can be seen in Group 3 and Group 4, where it is clear that the assignments of the groups have been switched but the composition is unchanged. (b) Corresponding plots for the gut data when trained to predict succinate using four groups (note that only two groups are used in Fig. 3g-h). (c) Corresponding plots for the ocean data when predicting nitrate. (d) Corresponding plots for the soil data when predicting nitrate dynamics.



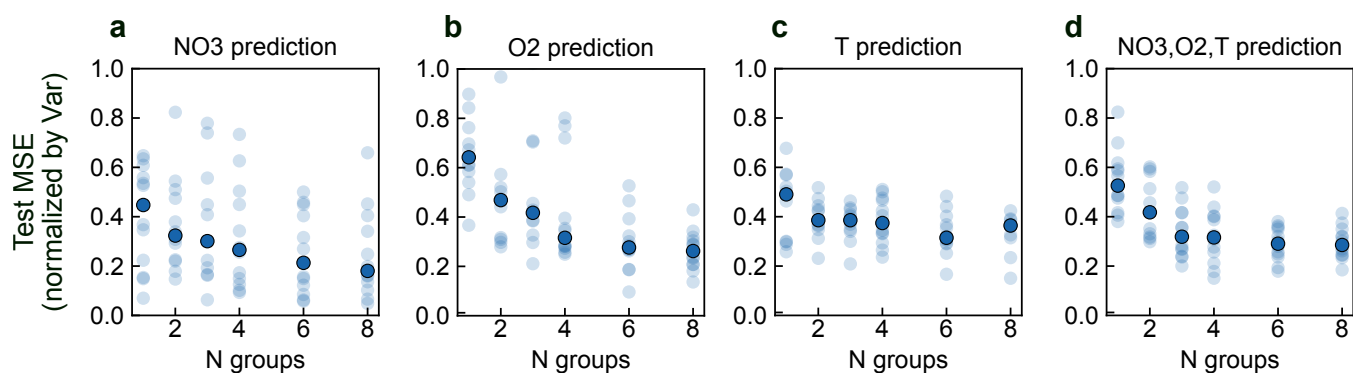
Supplementary Figure S7: Consistency of groups across hyperparameters. For each of the datasets in Fig. 3 we evaluate the sensitivity of the learned groups to hyperparameters used for model training (Methods). For each of these datasets we show three plots which follow the same structure. (a) R^2 values for each of the different hyperparameter sets, enumerated with Roman numerals. Small dots correspond to single models in the ensemble. The top models highlighted in red are used to determine the consensus grouping (Methods). (b) Consensus group composition resulting for each hyperparameter set. Each set of nodes (rectangles) in the flow diagram are aligned vertically with the corresponding hyperparameter set from (a). Each bar between nodes represents one species; its thickness corresponds to its average abundance. While the grouping is very stable for the synthetic gut data, it is less so for the ocean data (panels g-i). The hyperparameters corresponding to each set (I-III) are shown at the bottom of (b). (c) Confusion matrices to compare the group assignments across hyperparameter sets. Each matrix is a comparison between one set of hyperparameters (Roman numerals). Entry i, j in the matrix is the number of species that are assigned to group i for one hyperparameter set and to group j for another hyperparameter set. (d-f) Corresponding plots for the gut data with succinate concentration as the target function. (g-i) Corresponding plots for Tara oceans data with nitrate concentration as the target function. Blue species which were identified by the EQO method from Ref. [24] are highlighted in blue. In this data (as opposed to the synthetic gut data) there is more variation in the relevant (top) group which reflects the fact that the data is both more complex (higher dimensionality) and less sampled. Species colored in dark gray are ones that are sometimes, but not always, in the relevant group. (j-l) Corresponding plots for the soil data with nitrate dynamics as the target function.



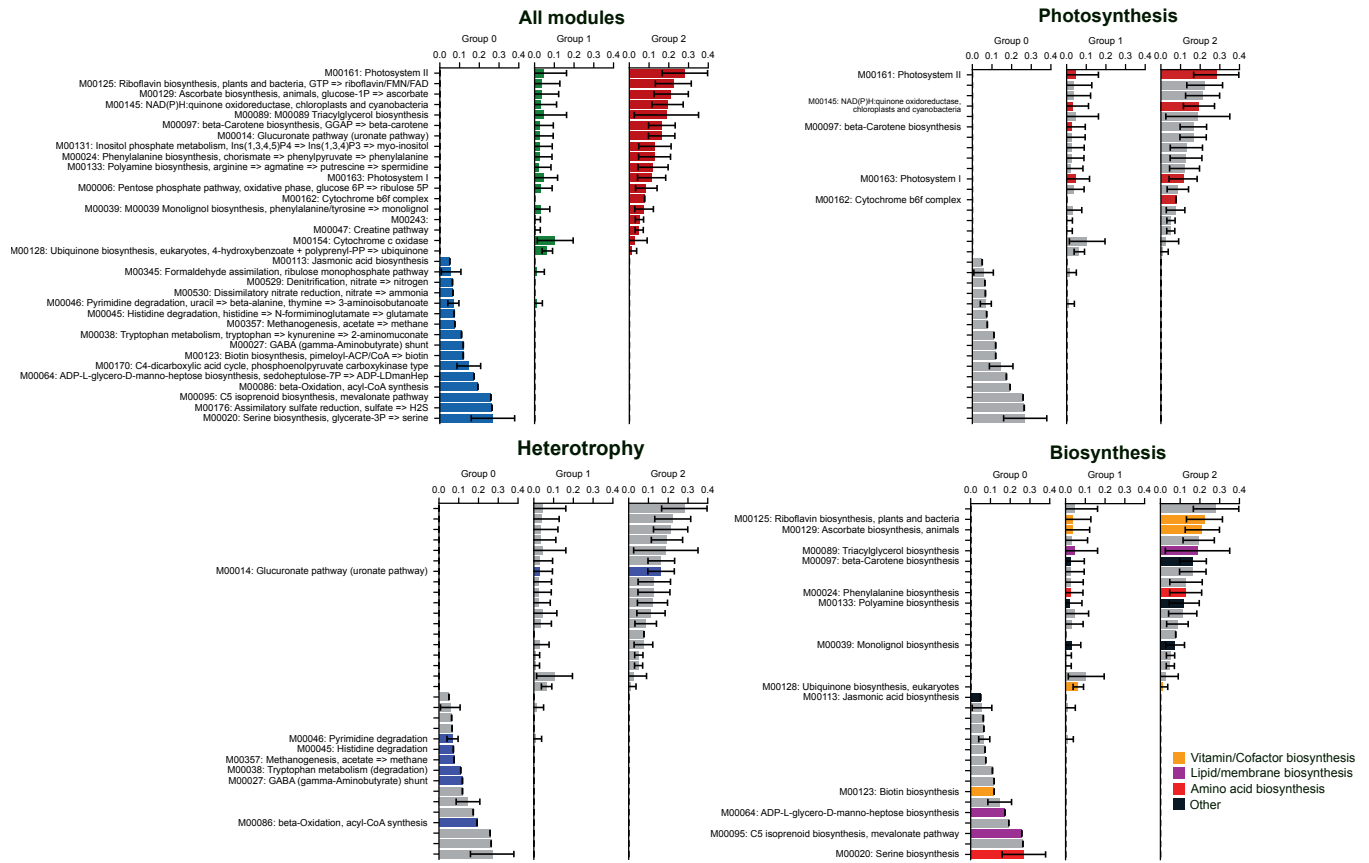
Supplementary Figure S9: Gut species abundances and correlations with pH. (a) Correlation of every species with pH in samples where that species was included. Samples with p value greater than 10^{-1} are on the right. Species in the “pH buffer group” are highlighted in green. (b) Average abundance of species across the dataset (not stratified by community richness). Species in the relevant succinate group are highlighted in brown.



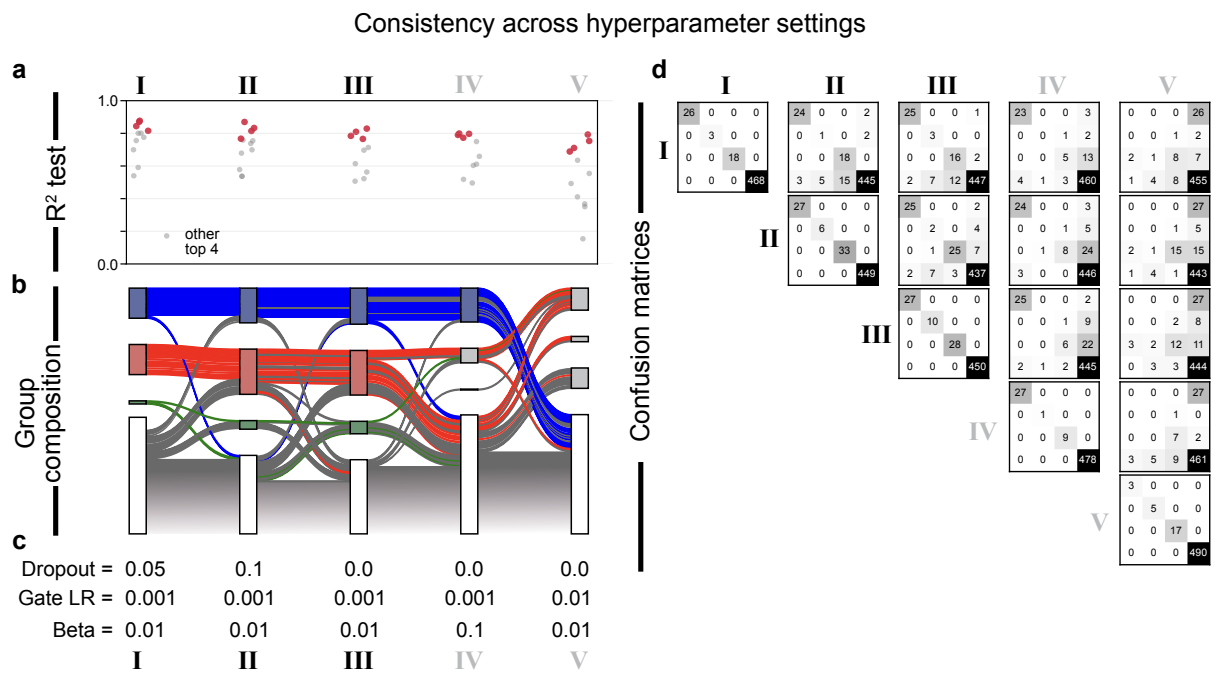
Supplementary Figure S10: Method comparison. Each row corresponds to one row (dataset) in Fig. 3. We compare SCiFI to five other approaches. For the clustering step, we consider either a co-occurrence network approach (Co-occ.), the clustering learned by SCiFI, or a linear function-informed clustering method that relies on a Metropolis-Hastings algorithm [25]. The co-occurrence clusters are either used to train a linear regression model (LR), corresponding to a Model I-type algorithm discussed the main text and Fig. 2, or to train a neural network (NN), corresponding to a Model II-type algorithm. In addition, we also consider a model which performs dimensionality reduction with principal component analysis (PCA). Left shows the R^2 of these six different models. The first three have linear structure-function maps, the last three are nonlinear. The bars show the average R^2 across the entire ensemble of models ($N_{\text{ens}} = 12-20$ depending on dataset), with individual points showing the R^2 for single models. Blue bars are function-informed. Dark blue denotes the two approaches that rely on SCiFI: either the full SCiFI algorithm (far right), or an approach which fully trains SCiFI but then discards the neural network structure-function map for a linear model. Light blue denotes the Metropolis-Hastings algorithm which is function-informed but linear. (a) For butyrate prediction in the gut community experiments of Ref. [32], SCiFI outperforms all other models except one which uses PCA and a neural network. This indicates nonlinearity is important, and that the dominant modes of covariance in abundance data are reflective of butyrate producers. (b) Group overlap (confusion matrices) between SCiFI and the Metropolis-Hastings algorithm (left) and between SCiFI and the co-occurrence network (right). Entry i, j in the matrix shows the number of species that were assigned to group i using one method and j using the other method. In this dataset, Metropolis Hastings recovers almost the same groups as SCiFI despite not making accurate predictions. (c-d) Same as (a-b) but for succinate prediction. (e-f) Same for the Tara Oceans dataset predicting nitrate. (g-h) Same for the prediction of nitrate reduction dynamics in soils. SCiFI is the only method that either matches or outperforms all other methods across every dataset.



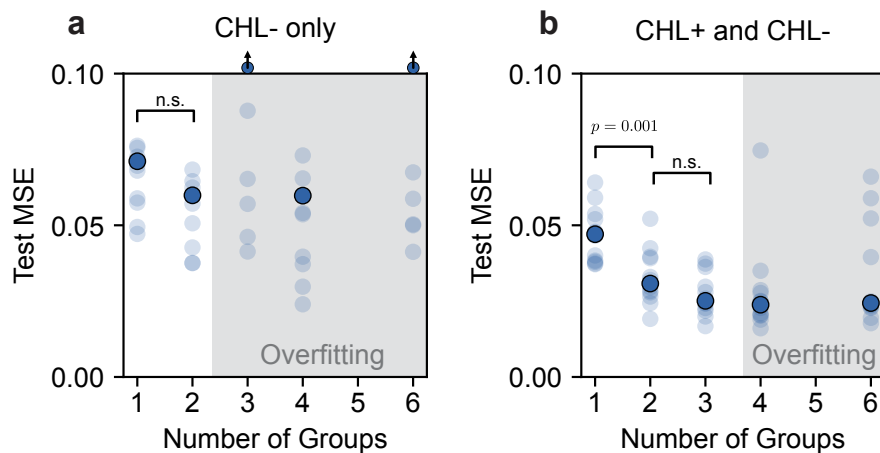
Supplementary Figure S11: Error dependence on number of groups for Tara Oceans metagenome Each panel shows the evolution of mean squared error (MSE) on a held-out test set for varying numbers of groups. MSE is normalized by the variance of the predicted function, so that a value of 1 corresponds to the error of a model which simply predicts the mean function value. As in Fig. 3, each faint dot corresponds to one model trained on one subset of the training data. Solid dots are the median over the ensemble of models. (a) Results when training SCiFI to predict nitrate concentration. Although the median decreases steadily with increasing numbers of groups, the variance is very large. (b) Results when predicting oxygen concentration. As with nitrate, the variance of model performance is large. (c) Results when predicting temperature. (d) Results when simultaneously predicting nitrate, oxygen, and temperature.



Supplementary Figure S12: Module-level cluster assignments for Tara metagenomics. Here we highlight individual modules isolated using function-driven clustering. Top left shows all KEGG modules with their full descriptions. The bar length is the average abundance of the module assigned to each cluster. This average is taken over samples, and over an ensemble of models (we compute the average only over the top 50% of models). Error bars show the standard deviation (truncated at 0) across the ensemble of models. Top right shows how modules related to photosynthesis are concentrated in group 2. Bottom left shows modules related to heterotrophy, which are mostly concentrated in group 0 with the exception of M00014 (Glucuronate pathway). Glucuronate is a precursor for building of extracellular polymeric substances (in bacteria) [39, 40]. It may also serve as a precursor to ascorbate in animals, suggesting that this may signal the presence of genetic material from eukaryotic plankton which use the protective effects of ascorbate [55]. Bottom right shows modules related to biosynthesis. These are distributed across groups 1 and 3. The surface group (group 3) contains modules used for protective structures (ascorbate, beta carotene, polyamines) and energetically-expensive structures (phenylalanine, monolignol). Riboflavin biosynthesis is important in the surface group because riboflavin degrades rapidly due to light [56], meaning it must be constantly generated to maintain the constant supply necessary for growth. The deep group (group 1) contains structures used in archaea (Mevalonate, ADP-heptose), simple amino acids (serine) and cofactors which are potentially useful for heterotrophy (biotin, used for anaplerosis).

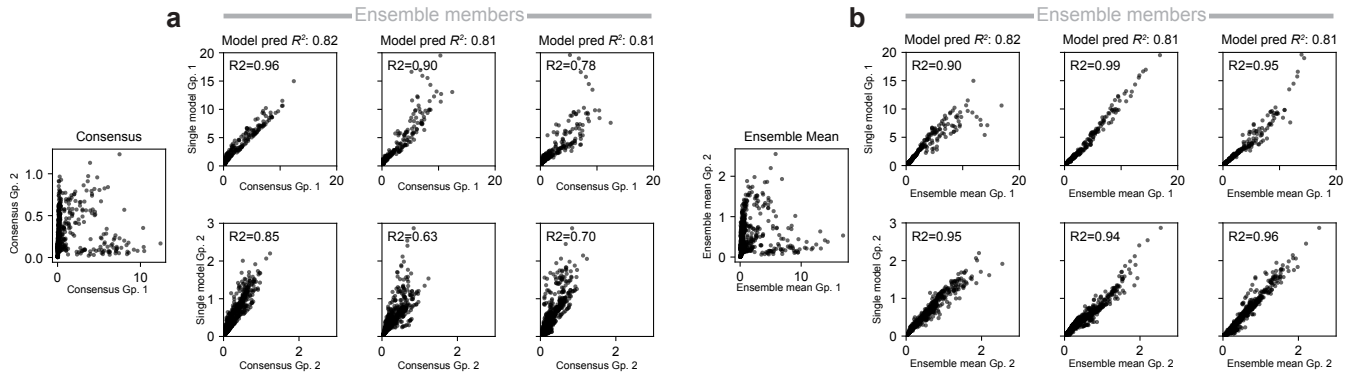


Supplementary Figure S13: Consistency of groups across hyperparameters: Tara metagenomics. Here we evaluate the sensitivity of the learned gene groupings from Fig. 4 to training hyperparameters. (a) R^2 values for each of the different hyperparameter sets, enumerated with Roman numerals. Small dots correspond to single models in the ensemble. The top four models highlighted in red are used to determine the consensus grouping (Methods). Performance is mostly constant for hyperparameter sets I-III but begins to degrade in IV and V. (b) Consensus group composition resulting for each hyperparameter set. Each set of nodes (rectangles) in the flow diagram are aligned vertically with the corresponding hyperparameter set from (a). Each bar between nodes represents one gene module; its thickness corresponds to its average abundance. The genes in each of the three groups from Fig. 4 are colored accordingly. The bottom group (gray) represents all genes that are removed by the gating procedure. These are not used as an input to the structure-function map neural network. (c) The hyperparameters corresponding to each set I-V. (d) Confusion matrices to compare the group assignments across hyperparameter sets. Each matrix is a comparison between one set of hyperparameters (Roman numerals). Entry i, j in the matrix is the number of genes that are assigned to group i for one hyperparameter set and to group j for another hyperparameter set.

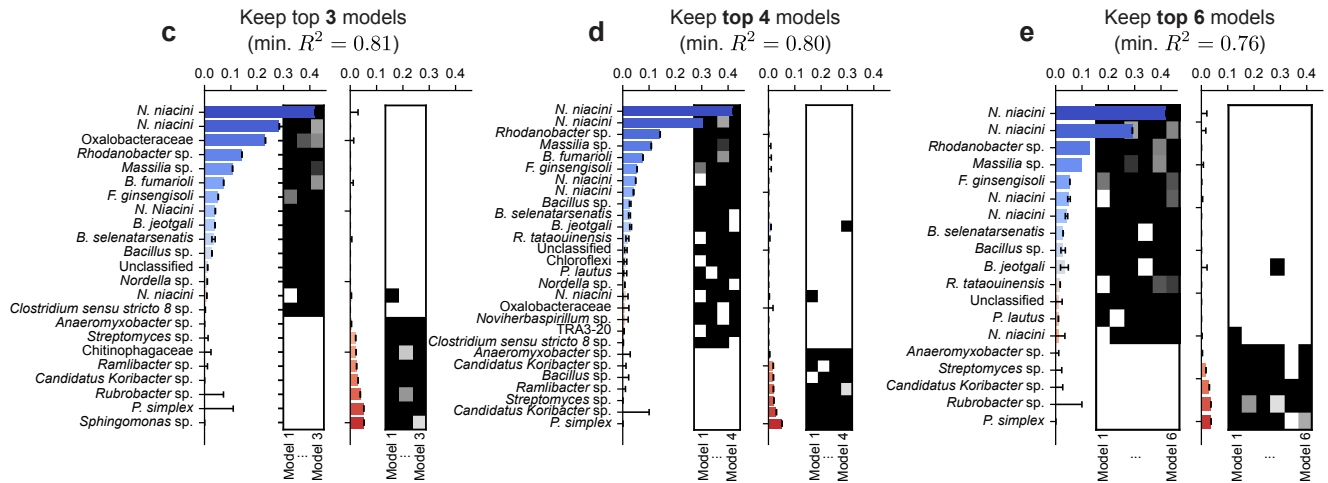


Supplementary Figure S14: Test (mean squared) error versus number of groups for soil data. Predictions are made with ASV-level abundance data as input, using only CHL-untreated samples (a) or both treated and untreated samples (b). Models are trained with the gating procedure described in Methods. Each semi-transparent point is one model trained with a different test-train split of the data. Solid point is the median loss. There are clear signs of overfitting for larger numbers of groups (gray background) because test error begins to grow rapidly. Note that some models with test MSE > 0.10 are not shown. Cases where the median MSE is greater than this value are shown with a point lying on top of the axis in (a). Parameters $lr = 10^{-3}$, $lr_{\text{gate}} = 10^{-1}$, $\beta = 10^{-2}$, $p_{\text{dropout}} = 0.05$. p -values shown for two-sided t-test comparing the means of the distribution of errors. Other differences are not significant (n.s.); for CHL- only the differences between 1 and 2 groups has $p = 0.28$ and for both treated and non-treated the difference between 2 and 3 groups is $p = 0.10$.

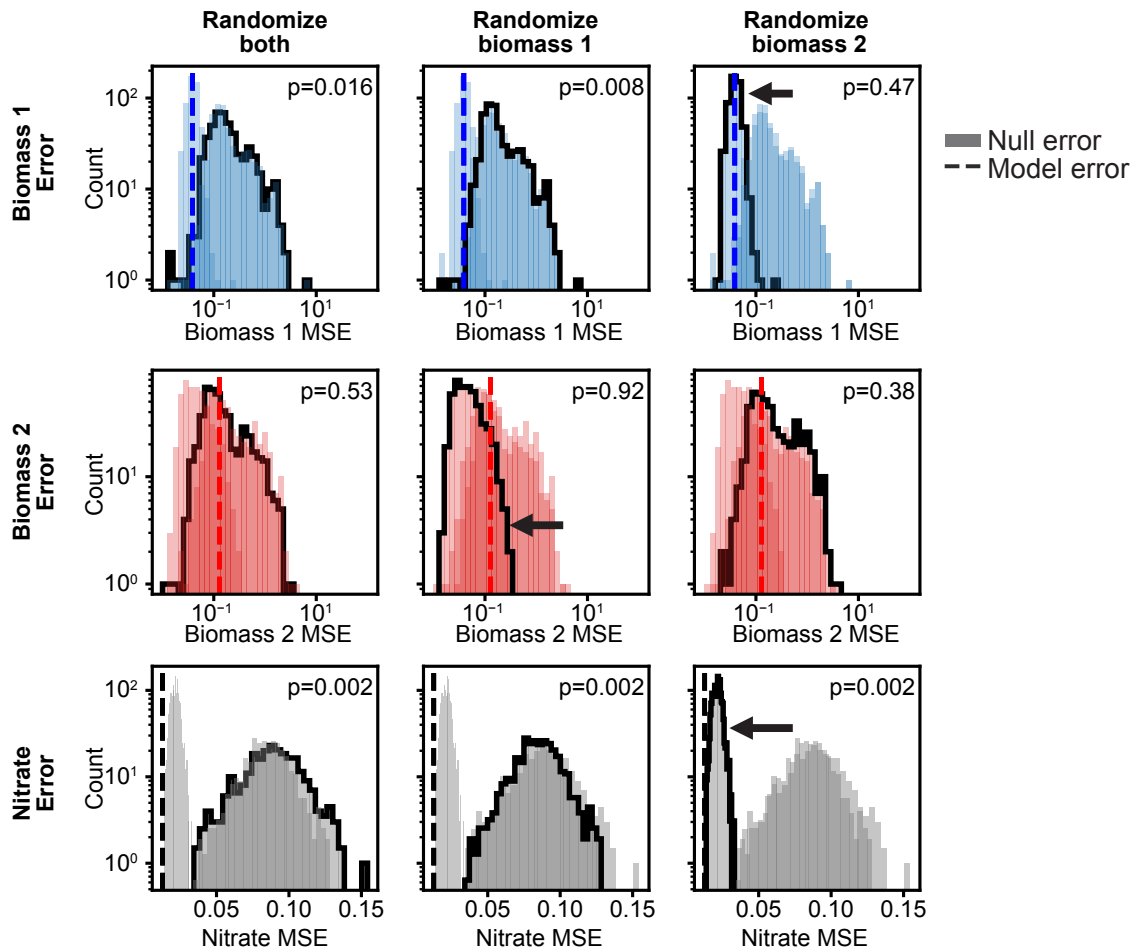
Consistency across models: Grouped abundances



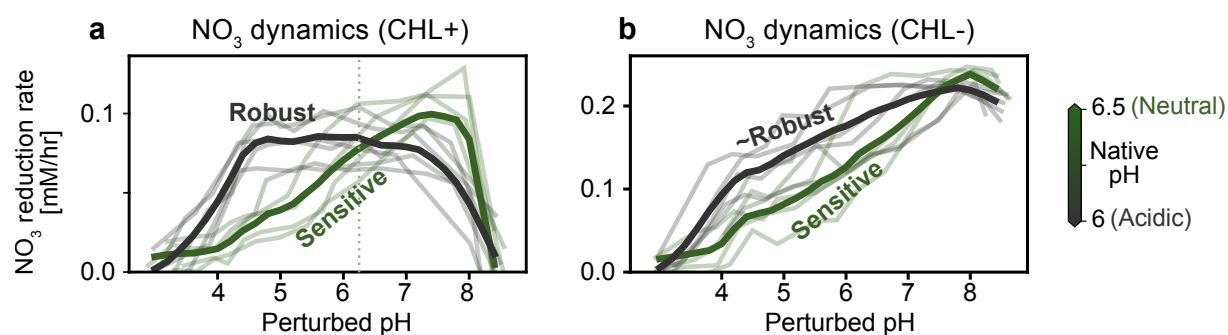
Consistency across models: Composition



Supplementary Figure S15: Learned assignments are consistent across different selection criteria. We train an ensemble of models, each of which may learn a different grouping. We explore two ways of determining “average” group abundances. First, we can take a “consensus grouping” which selects all species that are placed into a single group more than 50% of the time across the ensemble (see Methods). Second, we can first compute the group abundances for each ensemble member individually, and then compute the average across the ensemble. These give different results because in the first approach one neglects small or unimportant groups, while in the second they are taken into account because they contribute to the group abundance for each individual model. (a) Comparison of group 1 and 2 abundances (top and bottom row) for the individual models compared to the consensus group. (b) Comparison of individual model group abundances to the ensemble mean abundances. (c-d) Show how our selection of the consensus group members is stable whether we take the top 25% (3) of models or the top 50% (6) to build the consensus group. From this subset of models, a group member is included if it is present in 75% or more of the individual models. (c) Left axis shows the average end-point abundances (blue) of each species included in the consensus group. The inset matrix shows the presence of each species across all models. Right axis shows abundances (red) of species in Group 2. These species are all those included if we determine our consensus group from the top 3 performing models. (d) Consensus group members derived from the top 4 performing models, sorted by abundance (blue, red) with their presence/absence across models (inset matrices). (e) Consensus group members derived from the top 6 performing models.



Supplementary Figure S16: Null model comparison. A full description of the figure is found in Methods. Each row shows the distribution (highlighted in black) of errors using a null model of group abundances which draws either both groups from a null distribution (left column), only group 1 (middle) or only group 2 (right). Distributions from other null models are shown, not highlighted, for comparison. Top row shows error in biomass 1 end-point abundance prediction; middle shows error for biomass 2; bottom shows error for nitrate dynamics. p -values shown are the empirical probabilities of observing a null model error that is lower than the correct model error (shown with vertical dashed line). The arrows highlight some observations which are discussed in Methods.



Supplementary Figure S17: Nitrate reduction dynamics in CHL treated and untreated conditions. (a) Reproduction of Fig. 6c for comparison. (b) Nitrate reduction rate for each soil sample as a function of perturbed pH. As in Fig. 6c, each soil sample (faint lines) is colored by native pH. Solid lines show the average across acidic (pH < 6.25) and neutral (pH > 6.25) soils. The difference between robust and sensitive soils is less pronounced than in the CHL-treated samples but still present.